

# Consistent Interpretation of Electrical and Optical Transients in Halide Perovskite Layers and Solar Cells

Lisa Krückemeier,\* Zhifa Liu, Benedikt Krogmeier, Uwe Rau,\* and Thomas Kirchartz\*

Transient photoluminescence (TPL) and transient photovoltage (TPV) measurements are important and frequently applied methods to study recombination dynamics and charge-carrier lifetimes in the field of halide-perovskite photovoltaics. However, large-signal TPL and small-signal TPV decay times often correlate poorly and differ by orders of magnitude. In order to generate a quantitative understanding of the differences and similarities between the two methods, the impact of sample type (film vs device), large- versus small-signal analysis, and differences in detection mode (voltage vs. luminescence) are explained using analytical and numerical models compared with experimental data. The main solution to achieving a consistent framework that describes both methods is the calculation of a voltage or carrier density dependent decay time that can be interpreted in terms of a capacitive region, a region dominated by defect-assisted recombination and a region that is dominated by higher order recombination (radiative and Auger). It is experimentally shown that in the efficient methylammonium lead-iodide solar cells, effective monomolecular lifetimes  $\approx 2 \mu\text{s}$  can be consistently measured with TPL and TPV. Furthermore, the shape of the decay time versus voltage or carrier density follows predictions derived from implicit and explicit solutions to differential equations.

of recombination is a near obligatory ingredient of a huge number of scientific studies aimed at reducing nonradiative recombination in halide perovskites. Recombination affects the concentrations  $n$  and  $p$  of free electrons and holes. In most cases, charge-carrier concentrations are not directly measured. Instead, various observable quantities are measured as a function of time after photoexcitation, which are more or less closely related to the charge-carrier concentration. These measurable quantities include voltage,<sup>[1–3]</sup> luminescence,<sup>[4,5]</sup> conductivity<sup>[6–8]</sup> and the amount of free carrier absorption.<sup>[9,10]</sup> Sometimes, extracted currents in response to a laser pulse are measured as a (relatively) direct assay of charge carriers being extracted as a function of time.<sup>[11–15]</sup> Furthermore, time constants related to recombination are also extracted from frequency domain methods.<sup>[16–18]</sup> Among these different options, two rather common modes of detection in the field of halide perov-

## 1. Introduction

Nonradiative recombination is one of the most important loss mechanisms in any solar cell technology including the emerging technology based on halide perovskites. Hence, characterization


skite research are the measurement of the transient photoluminescence (TPL) applicable to layers, layer stacks and devices and the transient photovoltage (TPV), which—using electrical detection—requires complete solar cell devices. The PL signal during a TPL experiment is proportional to the product  $np$  of electrons and holes,<sup>[9,19]</sup> while the TPV as a small-signal measurement measures an excess voltage  $\Delta V$  that is assumed to be proportional to the laser-induced excess-carrier concentration  $\Delta n_{\text{laser}}$ .<sup>[14]</sup>

In both cases, it is common in the literature to report decay times that result from exponential fits to the TPL or TPV data. Figure 1 presents data collected from literature,<sup>[11,20–38]</sup> which compares decay times extracted from these two techniques plotted against each other. Figure 1 shows that the two decay times typically differ by up to four orders of magnitude with the correlation between the decay times being extremely poor. This level of discrepancy cannot easily be explained by the mode of detection alone. While there is an abundance of studies that uses both techniques to characterize perovskite films or devices,<sup>[11,20–38]</sup> a theory that connects the two decay times with each other is so far missing. The lack of understanding what these decay times mean, how they are related to each other and their variation by several orders of magnitude undermines the ability of the research community to understand and compare recombination and the concept of charge-carrier lifetimes.

In this paper, we will study and explain the discrepancies between the two methods and show that quantitatively

L. Krückemeier, Z. Liu, B. Krogmeier, U. Rau, T. Kirchartz  
IEK5-Photovoltaik  
Forschungszentrum Jülich  
52425 Jülich, Germany  
E-mail: l.krueckemeier@fz-juelich.de; u.rau@fz-juelich.de;  
t.kirchartz@fz-juelich.de

L. Krückemeier, U. Rau  
Faculty of Electrical Engineering and Information Technology  
RWTH Aachen University  
Mies-van-der-Rohe-Straße 15, 52074 Aachen, Germany  
T. Kirchartz  
Faculty of Engineering and CENIDE  
University of Duisburg-Essen  
Carl-Benz-Str. 199, 47057 Duisburg, Germany

 The ORCID identification number(s) for the author(s) of this article can be found under <https://doi.org/10.1002/aenm.202102290>.

© 2021 The Authors. Advanced Energy Materials published by Wiley-VCH GmbH. This is an open access article under the terms of the Creative Commons Attribution License, which permits use, distribution and reproduction in any medium, provided the original work is properly cited.

DOI: 10.1002/aenm.202102290

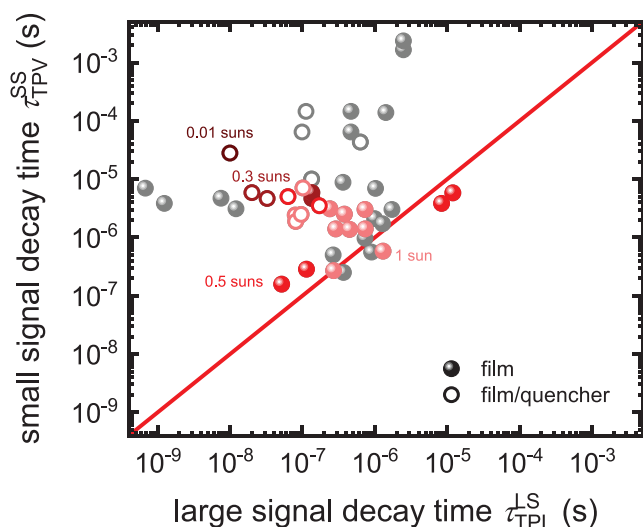


**Figure 1.** Data collection from literature, comparing the decay time  $\tau_{\text{TPL}}^{\text{LS}}$  of the transient PL measured on perovskite films (filled symbols) or on perovskite/transport layer stacks (blank symbols) with the stated decay time  $\tau_{\text{TPV}}^{\text{SS}}$  resulting from transient photovoltaic measurements on the respective solar cell device. The color code is linked to the bias light intensity during the TPV experiment ranging from light red (1 sun) to dark red (0.01 suns). For the grey data points, no information about the bias illumination level was available. The bisecting line (red) serves as a guide-to-the-eye and indicates where both decay times are equal. The comparison of these decay times highlights that they correlate poorly and can differ by orders of magnitude. Interestingly, the decay time constant from the TPV measurement is usually longer, although recombination losses are expected to be higher in the complete solar cell than in the pure perovskite film. The publications<sup>[11,20–38]</sup> from which the data were extracted are listed in Table S1 (Supporting Information).

consistent results are obtained if suitable measurement conditions and data analysis methods are used. We also explain the reasons, why the decay times can vary by orders of magnitude depending on the sample type and measurement condition and under which circumstances the decay times are actually related to recombination and the charge-carrier lifetime.

When looking at the literature data presented in Figure 1, one of the most obvious differences is that TPV is an electrical technique measured on devices, whereas TPL is typically measured on perovskite layers or layer stacks but rarely on full devices. While a perovskite layer has two surfaces that may potentially cause substantial recombination losses, the glass/perovskite interface is usually of high electronic quality and the perovskite surface can easily be passivated using insulating molecules such as TOPO (triethylphosphine oxide)<sup>[39]</sup> or APTMS (3-aminopropyl)trimethoxysilane.<sup>[40]</sup> In contrast, completed devices have additional layers and interfaces that have to support charge extraction and therefore cannot easily be passivated with electrically insulating molecules. Thus, one might expect that recombination in devices is always enhanced relative to a well-passivated perovskite film on glass and that therefore time constants in TPV on devices should generally be shorter than in TPL on films. However, Figure 1 shows that the opposite is true with decay times from TPV often drastically exceeding those measured from TPL. This may in part be due to the lack of good surface passivation for the films measured in TPL. However,

the major contribution will be the influence of slow capacitive effects that originate from the electrodes being discharged via the perovskite diode.<sup>[1,41–43]</sup> While the resulting long decay times are still related to recombination, they are much longer than the actual charge-carrier lifetimes of the bulk material.

In order to better understand the differences between the decay times, in the following, we briefly describe the two measurement methods. Subsequently, we present explicit and implicit solutions to the differential equations describing recombination as well as capacitive charging and discharging of the electrodes. We distinguish between large- and small-signal solutions to the equations and explain the differences in extracting effective Shockley–Read–Hall (SRH) lifetimes or radiative recombination coefficients from small- or large-signal decays. Finally, we show that an unambiguous interpretation of experimental data from completed perovskite solar cells is possible only when scanning a range of charge carrier densities (in TPL) or bias voltages (in TPV) that covers the capacitive charging/discharging regime at low and the radiative recombination regime at high injection conditions. Between these extremes, a window of intermediate carrier densities or voltages allows to identify the effective SRH lifetime<sup>[44,45]</sup> of the absorber and its interfaces to the contact materials.

## 2. Fundamentals

### 2.1. Introduction to the Methods

TPL and TPV measurements are used to monitor charge-carrier dynamics and to analyze recombination losses in the field of halide perovskite photovoltaics. Figure 2 provides an example of the setups for TPL (red) and TPV (blue). Both methods measure a transient response to a short laser pulse excitation. TPL detects the emitted photoluminescence  $\phi_{\text{TPL}} \sim np$  created by radiative recombination between a population of electrons and holes (with the concentrations  $n$  of electrons and  $p$  of holes) in the absorber material as a function of the delay time after this laser pulse. For detection, we typically use either a gated charge-coupled device (CCD) camera (as visualized in Figure 2) or a time-correlated single-photon counting (TCSPC) detection unit.<sup>[46]</sup> Given that radiative recombination originates from the perovskite layer itself, the measurement provides a measure of the recombination kinetics in the perovskite. The excess-charge carriers generated by the absorption of the laser pulse cannot leave the sample and have to recombine at some point. Since TPL is a purely optical technique, no electrical connection is necessary and it can be applied to any type of sample, from pure films on glass up to complete solar cell devices. Nevertheless, TPL on perovskites samples is mainly measured on pure films, because the interpretation of data obtained on multilayer samples is challenging due to the superposition of various effects that modulate the charge-carrier concentration in the perovskite layer and thereby the measured PL.<sup>[47–49]</sup> TPL measured on thin perovskite films on glass is a frequently used method to derive the recombination rate constants of trap-assisted SRH, radiative, and Auger recombination in the bulk material.<sup>[50–52]</sup> Given that TPL is generally performed as a large-signal (LS) method (i.e., without bias light), the decay is usually too complex to

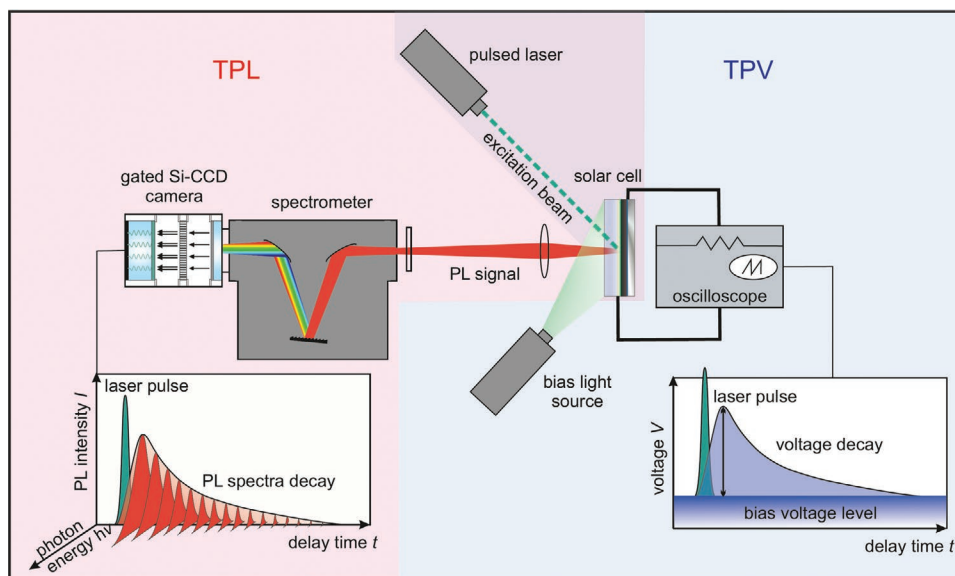


**Figure 2.** Schematic of the transient photoluminescence (TPL) (red) and transient photovoltage (TPV) (blue) setups. Both experiments require a pulsed laser that hits the sample. For TPV, a bias light illuminates the sample to perform a small signal measurement where the transient voltage signal is measured with an oscilloscope. In case of TPL, the photoluminescence is measured as a function of time, e.g., with a gated CCD camera (as shown here) or with a time correlated single-photon counting system.

be described by a single exponential. Instead, the decay time changes during the course of the transient and as a function of carrier concentration thereby reflecting the importance of different recombination mechanisms at different injection levels.<sup>[49]</sup> TPL data measured with a high dynamic range may span a large range of injection levels thereby providing carrier-concentration dependent information on recombination in a similar way as, e.g., quasi-steady state photoconductivity measurements of passivated crystalline Si wafers.<sup>[53,54]</sup>

In contrast, TPV is an external, electrical technique that requires contacts and that can only be applied to complete solar cell devices. Furthermore, TPV is a small-signal (SS) method during which the solar cell is kept in an excited state at open circuit by a permanent bias illumination. An additional weak laser pulse generates a small amount of additional excess-charge carriers, inducing a transient change in open-circuit voltage.<sup>[14,55]</sup> To record the photovoltage decay, the sample is electrically connected to an oscilloscope whose input impedance must be high ( $\approx M\Omega$ ) to ensure that the device is held under open-circuit condition. In order to obtain information at different injection levels, the TPV method requires using different bias light intensities.

**Figure 3** presents data from (a) transient PL and (b-c) transient photovoltage measurements on methylammonium lead iodide ( $\text{CH}_3\text{NH}_3\text{PbI}_3$ ) (MAPI) samples. The used layer stack is glass/ITO/PTAA/MAPI/PCBM/BCP/Ag for the solar cells and glass/MAPI/TOPO for the film on glass. Here, ITO is indium tin oxide, PTAA is poly(triarylamine), PCBM is [6,6]-phenyl- $\text{C}_{60}$ -butyric acid methyl ester and BCP is bathocuproine. In Figure 3a, the background corrected and normalized transient PL decay is shown for a MAPI layer on glass (grey) and a solar cell (red). The photoluminescence signal  $\phi_{\text{TPL}}$  is strongest directly after the laser pulse and decreases in intensity over time with the decay deviating substantially from a single

exponential decay. The state-of-the-art of interpretation of TPL decays of layer stacks or even full devices is currently still at an early stage. In experimental practice, the information contained in the decay curve is often reduced to one or two values—the characteristic decay time constants of a mono- or biexponential decay.<sup>[20–22,24–26,29,30,32–38,56]</sup> This reduction of the transient to two decay constants or even a single value will however cause a loss of information and impedes fully understanding and using the information contained in PL transients, as we will discuss later in Section 2.2.

TPV measurements are typically carried out at different bias light intensities. This light intensity often varies over orders of magnitude so that a large number of different operating points with different levels of open-circuit voltage can be investigated. Figure 3b shows a series of photovoltage decays at different illumination intensities, which gives an overview of how the shape of the decay changes depending on the bias level. Here, it becomes apparent that the decay time increases with reduced bias light intensity. The photovoltage transient due to the small laser perturbation is fitted to the slowest decay component using a monoexponential decay to obtain the small perturbation decay time constant  $\tau_{\text{TPV}}^{\text{SS}}$ , i.e.

$$\Delta V_{\text{oc}}(t) = \Delta V_{\text{oc,max}} \exp\left(-\frac{t}{\tau_{\text{TPV}}^{\text{SS}}}\right) \quad (1)$$

where  $\Delta V_{\text{oc,max}}$  is the maximum excess open-circuit voltage.<sup>[14]</sup> Instead of fitting the decay with Equation (1), one can also calculate  $\tau_{\text{TPV}}^{\text{SS}}$  from the derivative

$$\tau_{\text{TPV}}^{\text{SS}} = -dt/d \ln(\Delta V_{\text{oc}}(t)) \quad (2)$$

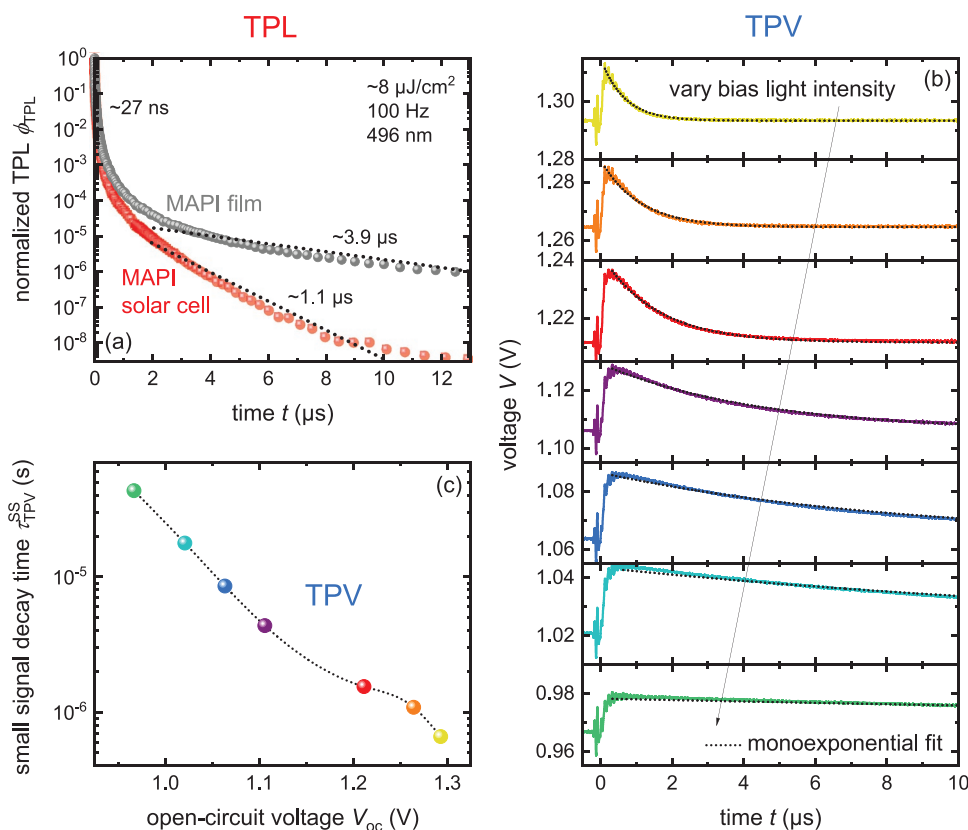


**Figure 3.** Comparison of an exemplary measurement of a) transient photoluminescence (TPL) and b,c) transient photovoltage and its common data analysis. a) TPL monitors the large-signal decay of photoluminescence intensity  $\phi_{\text{TPL}}$  over time after the sample is photoexcited by a short laser pulse. The slope at long delay times of the TPL signal is usually associated with SRH recombination and exponentially fitted to extract decay time constants. Respective fits are indicated as dotted, black lines for two different sample types, namely a complete solar cell (red) and its passivated perovskite absorber film (grey). TPV (b) is a small-signal method which is performed at open circuit for different steady-state bias illumination intensities. An additional weak laser pulse creates a small perturbation and generates a small amount of extra excess-charge carriers, inducing an additional open-circuit voltage. Then the corresponding photovoltage decay is measured and fitted with a monoexponential decay (dotted lines) to obtain the small perturbation lifetime associated with the steady-state  $V_{\text{oc}}$ . The time constants from the monoexponential fits are summarized in (c) for the different open-circuit voltages.

The different TPV lifetimes obtained at varying bias illuminations are then typically plotted as a function of the open-circuit voltage corresponding to the bias illumination as displayed in Figure 3c. To help understanding the different measurement principles and measurement conditions, we will briefly explain the different observables in transient photoluminescence and photovoltage measurements using the simulated band diagrams shown in **Figure 4**. These transient simulations were conducted with TCAD Sentaurus by Synopsys, which uses the finite element method to solve three partial differential equations, namely the continuity equations for electron and holes and the Poisson equation (for more details see Supporting Information). We simulated an inverted, planar perovskite ( $\text{CH}_3\text{NH}_3\text{PbI}_3$ , MAPI) solar cell with poly(triarylamine) (PTAA) as hole transport layer (HTL) and [6,6]-phenyl- $\text{C}_{61}$ -butyric acid methyl ester (PCBM) as electron transport layer (ETL). BCP was not explicitly simulated but we assumed that it reduces the workfunction of the Ag contact<sup>[57,58]</sup> to improve the built-in voltage and reduce the injection barrier for electrons at the Ag/PCBM contact. The device structure corresponds to the one used for the experimental data in Figure 3. The band diagrams on the left-hand-side of Figure 4 belong to the TPL situation

(no bias light), the ones on the right to the TPV measurement condition at different delay times (with bias light). The band diagrams from the TPL simulation belong to the same simulation series that was previously published in ref. [49]. Figure 4a,b depicts the respective band diagram for the initial situation before the laser pulse impinges on the sample. The comparison of these two band diagrams already shows a decisive difference between the two methods. In TPL, the sample is in equilibrium in the dark, which can be recognized by the equilibrium Fermi level  $E_{\text{F}}$ , before it is excited by the laser beam. The solar cell in the TPV situation, however, is already in an excited, stationary state due to the illumination with bias light (0.1 suns), causing an internal quasi-Fermi level splitting and externally measurable voltage of 1.21 V. Here,  $E_{\text{Fn}}$  denotes the quasi-Fermi level for electrons and  $E_{\text{Fp}}$  the one for holes, furthermore  $E_{\text{C}}$  and  $E_{\text{V}}$  mark the edges of the conduction and valence band as a function of the position  $x$ . Figure 4c,d shows the band diagrams directly after the laser pulse excitation. For TPV, only a small laser fluence is used to meet the small perturbation condition therefore the increase in Fermi-level splitting  $\Delta E_{\text{F,int}} = qV_{\text{int}}$  in the perovskite is hard to recognize, whereas in the TPL experiment the huge change from zero to 1.55 eV is directly visible.

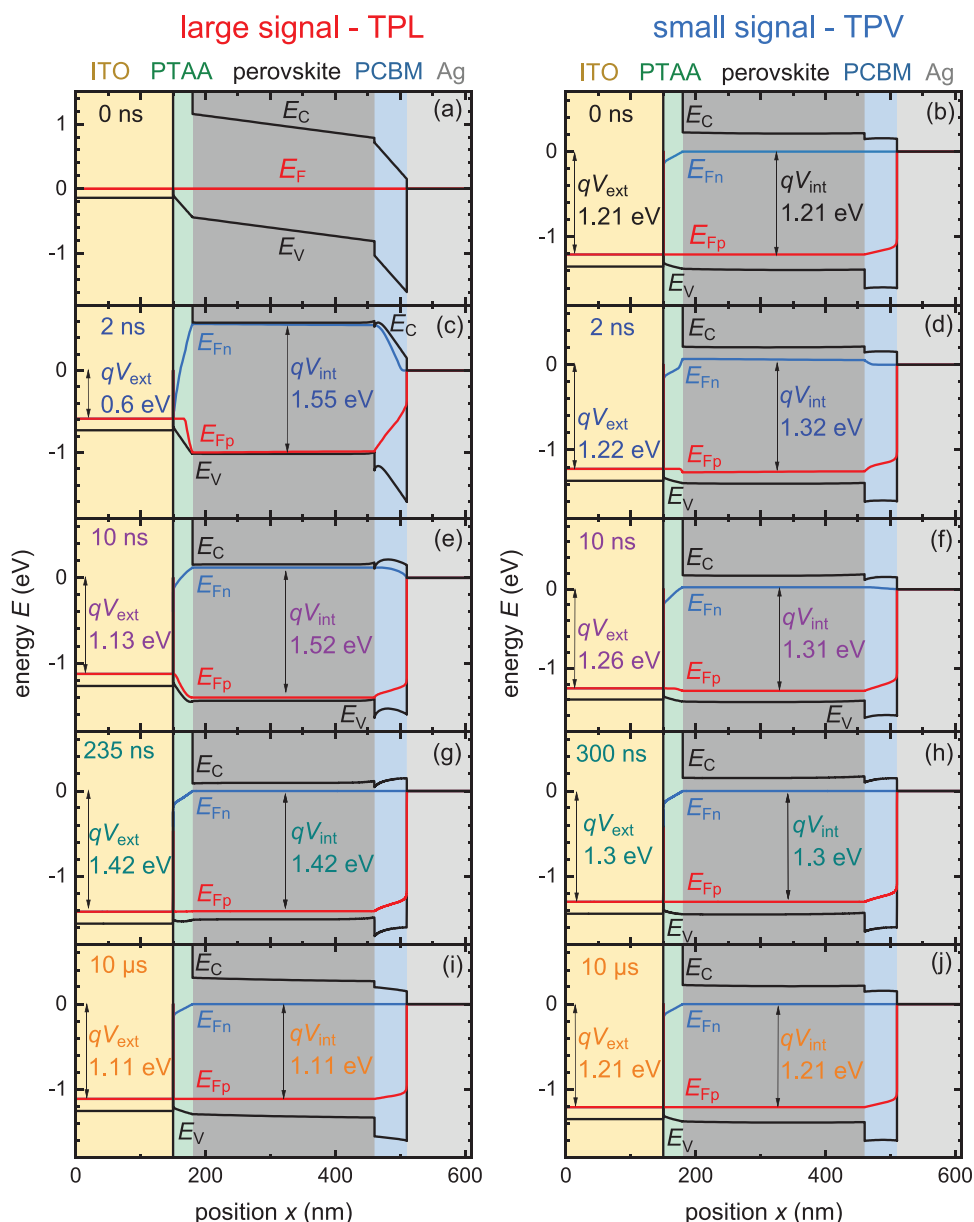


**Figure 4.** Band diagrams of a perovskite solar cell simulated with Sentaurus TCAD before and at different time delays after the laser pulse excitation for a large-signal experiment (right) compared to a small-signal experiment with bias light (left). a,b) Situation before the sample is photoexcited by the laser pulse ( $10 \mu\text{J cm}^{-2}$  for TPL,  $100 \text{ nJ cm}^{-2}$  for TPV). In the large-signal (TPL) experiment the sample is initially in the dark as can be seen from the equilibrium band diagram. In contrast to this, in the small-signal (TPV) experiment, the sample is kept at open circuit at a certain bias light intensity before the laser excitation. (c) and (d) show the situations directly after the end of the laser pulse, when the quasi-Fermi-level splitting in the perovskite is the highest but a negligible density of electrons has been transferred to the charge-transfer layers (PTAA, PCBM). In (e) and (f), substantial transfer of electrons to the PCBM has happened resulting in electron accumulation and band bending in the PCBM close to the perovskite/PCBM interface. g,h) Several hundreds of ns after the laser pulse the Fermi-levels are flat and the internal and external Fermi-level splittings are now similar. i,j) After  $10 \mu\text{s}$ , this band bending has vanished again, and the Fermi-level splitting has visibly decreased. The sample in the TPV experiment is back to its initial steady state, which is set by the bias light. The Fermi-level splitting in the TPL experiment will decrease further, since the charge carriers generated by the laser pulse continue to recombine and no new charge carriers are generated.

In both cases, it takes some time for the charge carriers created in the absorber to spread over the entire solar cell and reach the external contacts.

Therefore, the external voltage  $V_{\text{ext}}$  has not changed significantly yet compared to the change in internal voltage. There is a gradient  $dE_{\text{Fn}}/dx$  and  $dE_{\text{Fp}}/dx$  in the quasi-Fermi levels inside

the electron and hole transport materials, which drives the electron-  $J_n = n\mu_n dE_{\text{Fn}}/dx$  and hole-current density  $J_p = p\mu_p dE_{\text{Fp}}/dx$  from the absorber to the contacts to change the amount of charge stored on the electrodes. How fast this equilibration takes place depends on the transfer velocity and mobility of the contact layer materials, as well as on the capacitance of the



**Table 1.** To simplify the complexity of solving a system of partial differential equations in position and time, we present analytically solvable differential equations in this chapter that use various simplifications that help break down the problem into the most important elements. The main simplifications used are presented in the following. ODE: ordinary differential equation.

Complication/Effect	Significance	How to deal with it
Auger recombination	Important for perovskite solar cells at high fluences. <sup>[50,63]</sup>	Can be quite easily implemented in the solutions to the ODEs. See Table S3 (Supporting Information).
Doping	Of low relevance for our samples (see Supporting Information, Section 4). <sup>[64,65]</sup> However, it can be quite relevant for other perovskite samples, as seen, e.g., in ref. [61].	The equations can be written down easily for low level injection ( $\Delta n \ll$ doping concentration). However, for a case that extends from high to low level injection, there is probably no simple analytical solution.
Ions	Ions have been shown to affect some TPV measurements. <sup>[66]</sup> So far not much is known about their effect on TPL.	It is likely impossible to include them into a simple analytical description of these decays. In situations, where ions are important, numerical methods would have to be used.
Photon recycling	Generally important to understand the meaning of the radiative recombination coefficient.	Can be accounted for by using an “effective” radiative recombination coefficient that is corrected for the effect of photon recycling as discussed, e.g., in ref. [50,67].
Shallow traps, band tails	Shallow traps or band tails could cause SRH recombination with a low ideality factor close to 1. <sup>[68]</sup> In our model they would behave similar to radiative recombination.	In the logic of our model, a (nearly) quadratic recombination term could be accounted for by increasing the bimolecular recombination coefficient.
Noninteger ideality factors	Ideality factors that are neither close to 1 nor close to 2 over a range of voltages <sup>[69]</sup> would affect the shape of the decay time vs $\Delta E_F$ plots.	This can be implemented in the model. See Table S4 (Supporting Information).
Transport effects in absorber and contact layer	Finite mobilities could matter especially in low mobility (often organic) transport layers <sup>[70,71]</sup> but also in the perovskite itself. Very important, e.g., in organic solar cells. <sup>[72]</sup>	This would affect, e.g., the photovoltage rise <sup>[3,73]</sup> and could also affect the TPL and TPV decays if the effect gets sufficiently dominant. It cannot be implemented in a model based on a single ODE. Numerical models are needed.

electrodes. In this example it takes several hundred ns with the corresponding band diagrams being depicted in Figure 4g,h. At this point in time, the gradients  $dE_{Fn}/dx$  and  $dE_{Fp}/dx$  are nearly zero indicating that there is very little current flow to or from the electrodes and the internal and external voltage are equal. However, the charge-carrier concentration in the perovskite was not only reduced by charge transfer to the other layers, charging up the electrodes and changing the surface-charge density on cathode and anode, but also by recombination.

This delayed alignment between the internal and external state of the solar cell can affect the result of the measurement and can make data interpretation even more difficult. However, in this study we focus on the behavior of the decays at longer times where the assumption of equilibrated Fermi levels over the contact layers is more likely to be accurate than at shorter times. Furthermore, as we will show later, these long-term decays behave experimentally in a way that is fairly consistent with equilibrated Fermi levels as seen in Figure 4g–j). However, we note that this is not necessarily the case and Fermi-level gradients could in principle also happen at longer times during these small- and large-signal decays if the conductivity of the contact layers is relatively low and the layers are relatively thick.

In addition, strong band bending can be observed in the band diagrams, which is caused by charge accumulation near the interfaces. All these different effects superimpose and will influence the TPL signal.<sup>[49]</sup> With regard to the TPV, it should be noted that the maximum external voltage (1.3 V) is only reached after 300 ns, but some excess-charge carriers have already recombined before the actual decay of the photovoltage has even begun. The last two band diagrams show the situations for TPL (Figure 4i) and TPV (Figure 4j) after 10  $\mu$ s. The solar cell in the TPV experiment is back in its initial state, which is determined by the steady state illumination. The

Fermi-level splitting in the TPL situation continues to decrease. The electrons and holes flow back from the electrodes through the ETL and HTL to the perovskite. This process depends on the RC time constant with the capacitance  $C$  being formed by the electrode capacitance and the resistance  $R = dV_{ext}/dJ$  being determined by the recombination resistance of the solar cell that increases exponentially toward smaller voltages as predicted by the diode equation.

## 2.2. Description of Charge-Carrier Recombination in Films

In order to compare the meaning of the decay times extracted from the two experimental methods, we first need to establish the key differences between the methods and understand their impact on the decay. TPV and TPL are different in potentially three major aspects: i) The sample type (single layer, layer stack, full device), ii) the type of perturbation (large-signal vs small-signal analysis), and iii) the mode of detection (either optical or electrical). TPV is a method that requires full devices, uses a small-signal analysis and measures a voltage transient. TPL is a method that can in principle deal with any type of sample (with or without contacts) but is so far mostly used on films. Furthermore, TPL is nearly always performed as a large-signal measurement and it detects photons rather than an electrical voltage signal. In order to understand the impact of these differences on the decay times, we will establish and solve ordinary differential equations in time. We will start with films, continue to devices while in both cases discussing the differences between large- and small-signal analyses. Finally, we discuss the impact of the different observables (voltage and luminescence) on the decay times.

The numerical simulations used for Figure 4 are based on the solution to the time- and position-dependent drift-diffusion

equations for electrons and holes, a method that is intricate and time-consuming. Therefore, we aim at this point at a simple zero-dimensional recombination model without any influence of transport. Note that our simplification also assumes that charge transport within the absorber is fast relative to recombination. With these assumptions we arrive at a set of equations that can be solved analytically (see Table S2, Supporting Information). Note that Table 1 presents an overview of the different effects that we neglect in this model. Table 1 also comments on the significance of the different effects for halide perovskite-based samples and discusses in how far the effect can be included in analytical or numerical models.

### 2.2.1. Large-Signal Case

Since lead-halide perovskite films are often but not always intrinsic enough<sup>[59,60]</sup> that during a TPV or TPL experiment both carrier types are present in approximately the same concentrations, we assume that the high-level injection (HLI) condition ( $n = p$ ) is appropriate. We therefore use the HLI condition in the following but want to point out that this condition may not be met in certain samples<sup>[61]</sup> and would completely alter the shape of the decay. In the other limiting case of low-level injection, all recombination rates would be linear in minority-carrier concentration and in consequence decays would be monoexponential at least in films and would behave as described in ref. [62] in the case of complete cells.

We start with the case of a large-signal experiment performed on a perovskite film on glass, where recombination, expressed by its rate  $R(n)$ , is the only process that changes the charge-carrier density after a laser pulse excitation. In this case, the time-dependent charge-carrier concentration  $n(t)$  is determined by

$$\frac{dn(t)}{dt} = -R(n) = -k_{\text{rad}}(n(t)^2 - n_i^2) - \frac{\Delta n(t)}{\tau_{\text{SRH}}^{\text{eff}}} \quad (3)$$

where  $k_{\text{rad}}$  is the external radiative recombination coefficient and  $\tau_{\text{SRH}}^{\text{eff}}$  is the nonradiative SRH<sup>[44,45]</sup> effective lifetime with  $\tau_{\text{SRH}}^{\text{eff}} = (1/\tau_{\text{SRH}}^{\text{bulk}} + 1/\tau_{\text{SRH}}^{\text{surf}})^{-1}$  accounting for the bulk lifetime  $\tau_{\text{SRH}}^{\text{bulk}} = \tau_n + \tau_p$ , i.e., the sum of the electron and hole lifetimes, and the surface recombination related lifetime  $\tau_{\text{SRH}}^{\text{surf}}$ . Furthermore, we use the equilibrium concentration  $n_i$  (assumed equal for electrons and holes) and the excess carrier density  $\Delta n = n - n_i$ . In the remainder of the article, we will assume that we deal with situations, where  $\Delta n \gg n_i$  and hence  $\Delta n \approx n$  is a good approximation. This will simplify further equations slightly. In addition, we have omitted Auger recombination from Equation 3—again for the sake of keeping the equations simpler and more comprehensible—but it could be included in our concept (see Table S3, Supporting Information). Equation 3 is an ordinary differential equation in time as opposed to the set of partial differential equations (in space and time) that we have previously used to generate the band diagrams in Figure 4. Equation 3 has an explicit analytical solution for  $n(t)$  stated in Table S2 (Supporting Information). However, instead of using the detour via the explicit solution of Equation 3, it is advantageous to use implicit solutions that directly provide the decay time. In this case (large signal, film), the dependence of

the large-signal carrier concentration decay time  $\tau_{\text{film,HLI}}^{\text{LS}}$  on the actual carrier concentration  $n$  is given by

$$\tau_{\text{film,HLI}}^{\text{LS}} = -\frac{n(t)}{dn(t)/dt} = \frac{1}{k_{\text{rad}}n(t) + 1/\tau_{\text{SRH}}^{\text{eff}}} \quad (4)$$

where  $t$  is the time that passed after the end of the laser pulse. Thus, even without calculating  $n(t)$ , we can directly write down the relation between the decay time, the carrier density and the parameters  $k_{\text{rad}}$  and  $\tau_{\text{SRH}}^{\text{eff}}$ . Note that Equation (4) gives the decay time  $\tau_{\text{film,HLI}}^{\text{LS}}$  as a function of carrier density  $n(t)$  which varies as a function of time and hence  $\tau_{\text{film,HLI}}^{\text{LS}}$  could be presented both as a function of time or as a function of carrier density.

### 2.2.2. Small Signal Case

If a bias illumination is present, we must take the steady-state generation rate  $G$  of excess-charge carriers into account. Therefore, the differential equation in Equation (3) must be adjusted for the small-signal situation and it follows that

$$\frac{dn(t)}{dt} = -R(n) + G = -k_{\text{rad}}n(t)^2 - \frac{n(t)}{\tau_{\text{SRH}}^{\text{eff}}} + G \quad (5)$$

Due to the bias illumination, the carrier density  $n(t) = n_{\text{bias}} + \Delta n_{\text{laser}}(t)$  could be split up into two contributions, namely the steady state carrier density  $n_{\text{bias}}$  at a given bias photogeneration rate  $G$  and the additional time dependent part given by  $\Delta n_{\text{laser}}(t)$ . The small signal decay time  $\tau_{\text{film,HLI}}^{\text{SS}}$  at a given carrier concentration  $n_{\text{bias}}$  is then given by

$$\tau_{\text{film,HLI}}^{\text{SS}} = \frac{1}{dR/dn} = \frac{1}{2k_{\text{rad}}n_{\text{bias}} + 1/\tau_{\text{SRH}}^{\text{eff}}} \quad (6)$$

In order to compare large-signal and small-signal decay times, we need only one decay for the large-signal case but many small-signal decays measured at different bias levels represented by the parameter  $n_{\text{bias}}$  in Equation (6). Comparing the implicit expressions for the large- and the small-signal decay times  $\tau_{\text{film,HLI}}^{\text{LS}}$  and  $\tau_{\text{film,HLI}}^{\text{SS}}$ , Equations (4) and (6), we see that the decay times are only equal in the linear regime of  $R(n) \approx n/\tau_{\text{SRH}}^{\text{eff}}$  and differ by a factor of 2 once radiative recombination dominates the decay. This factor would go up to 3 in the case that Auger recombination would dominate (see Table S3, Supporting Information). This behavior is also reproduced by the explicit solutions of Equations (3) and (4) (Table S2, Supporting Information). Note that in the current literature on perovskites<sup>[1]</sup> it is sometimes stated that the small-signal and large-signal approaches lead to similar solutions, which is not correct in general and also especially not for perovskites where nonlinear radiative terms will dominate at higher voltages and carrier densities. In contrast, the fact that small signal- and large-signal decay times are different by a factor (often called reaction order) as long as recombination rates are nonlinear in carrier concentration is a well-known fact in the literature dealing with TPV transients in organic or dye-sensitized solar cells.<sup>[73–76]</sup>

Figure 5a–c summarizes our findings from the above comparison of the large- and small-signal measurement mode for

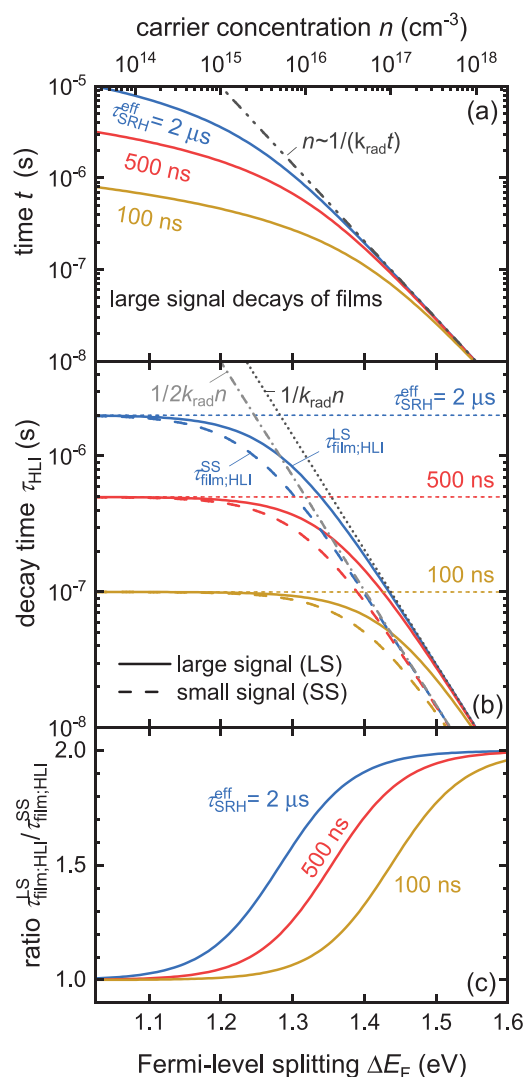


**Figure 5.** a) Transients  $n(t)$  calculated from the explicit solution (Table S2, Supporting Information) for Equation (3) representing recombination without surface or interface charging, typically measured on a bare film. Parameters are given in Table 2. Note that the time-axis is in y-direction and the transients start out of the lower right side of the graph from an initial value of  $n(0) = 10^{20}$  cm<sup>-3</sup>. The lower axis is the Fermi-level splitting  $\Delta E_F$  and the upper axis represents the charge-carrier concentration  $n$ , both quantities are related by Equation (7). The gray dashed line represents the asymptotic behavior of all three curves toward small times and high carrier concentrations which is dominated by radiative recombination with  $n(t) \propto 1/t$ . Only, at lower values of  $n$ , the individual curves are dominated by the different effective lifetimes  $\tau_{\text{SRH}}^{\text{eff}}$ . b) Comparison of large-signal decay times  $\tau_{\text{film,HLI}}^{\text{LS}}$  (full lines) and the small signal decay times  $\tau_{\text{film,HLI}}^{\text{SS}}$  (dashed lines) as a function of  $\Delta E_F$  (lower axis) or carrier concentration  $n$  (upper axis). The data are described by the implicit Equations (4) and (6) for the large and the small signal case, respectively. It is readily seen that both measured decay times  $\tau_{\text{film,HLI}}^{\text{LS}}$  and  $\tau_{\text{film,HLI}}^{\text{SS}}$  approach the respective effective lifetimes  $\tau_{\text{SRH}}^{\text{eff}}$  toward low values of  $n$  or small  $\Delta E_F$  (short dashed lines), whereas at higher values all large-signal curves converge with  $\tau_{\text{film,HLI}}^{\text{LS}} = 1/(k_{\text{rad}} n)$  and the small signal curves with  $\tau_{\text{film,HLI}}^{\text{SS}} = 1/(2k_{\text{rad}} n)$ . Thus, at the transition from nonradiative to dominant radiative recombination the ratio  $\tau_{\text{film,HLI}}^{\text{LS}}/\tau_{\text{film,HLI}}^{\text{SS}}$  between large and small signal decay times shifts from unity to two, as shown in panel (c).

**Table 2.** Parameters used for Figures 5 and 6.

Parameter	Unit	Value(s)
SRH lifetime $\tau_{\text{SRH}}^{\text{eff}}$	μs	0.1, 0.5, 2
Radiative recombination coefficient $k_{\text{rad}}$	cm <sup>3</sup> s <sup>-1</sup>	10 <sup>-10</sup>
Capacitance per area $C_{\text{area}}$	nF cm <sup>-2</sup>	50
Thickness	nm	280
Intrinsic carrier concentration $n_i$	cm <sup>-3</sup>	$8.05 \times 10^4$
Initial carrier concentration $n(t = 0)$	cm <sup>-3</sup>	10 <sup>20</sup>

the scenario of a perovskite film with SRH and radiative recombination being present. Figure 5a shows the result of solving the explicit solution of Equation (3) as shown in the Supporting Information. The solid lines represent the large-signal solutions for  $n(t)$  for three different SRH lifetimes (100 ns, 500 ns, 2 μs) and the dashed line represents the radiative limit given by infinite SRH lifetimes. Instead of using the common approach of showing  $n$  as a function of time  $t$ , we switched the  $x$  and  $y$ -axes for better comparison with Figure 5b showing the decay times  $\tau_{\text{film,HLI}}^{\text{LS}}$  and  $\tau_{\text{film,HLI}}^{\text{SS}}$  computed via Equations (4) and (6) as a function of carrier density. Furthermore, we use two  $x$ -axes for both panels. The top  $x$ -axis represents the carrier density  $n(t)$  in the large-signal case and  $n_{\text{bias}}$  in the small-signal case. The bottom  $x$ -axis is the associated Fermi level splitting  $\Delta E_F$  which is linked to the carrier densities via

$$\Delta E_F = k_B T \ln \left( \frac{n^2}{n_i^2} \right) \quad (7)$$

where  $n_i$  is the intrinsic charge-carrier concentration and  $k_B T$  the thermal energy. Note that we use the Boltzmann approximation (Equation 7) for relating carrier density and quasi-Fermi level splitting (QFLS) throughout the whole carrier density range for simplicity. When the QFLS approaches the band gap, Boltzmann will stop working and lead to deviations from Equation (7). The solid lines in Figure 5b result from large-signal decays, whereas the symbols are the small-signal solutions with each data point representing a different bias level. It is directly apparent that the small- and large-signal decay times change with charge-carrier concentration as predicted by Equations (4) and (6). Furthermore, two regions can be identified in each decay-time curve, whereby the decay time is constant at low carrier concentrations or low  $\Delta E_F$  and transitions to shorter values by decreasing exponentially with higher charge-carrier concentration or higher  $\Delta E_F$ . This plateau value at low  $n$  or  $\Delta E_F$  approaches the effective SRH lifetime  $\tau_{\text{SRH}}^{\text{eff}}$ . At high charge-carrier concentrations, higher-order recombination mechanisms, in this example radiative recombination, dominate and define the shape of the large- and small-signal decay times. The variation of the external radiative recombination coefficient  $k_{\text{rad}}$ , as done in the Figure S2 (Supporting Information) illustrates this in more detail. Furthermore, we recognize that the respective  $\tau_{\text{film,HLI}}^{\text{SS}}$  and  $\tau_{\text{film,HLI}}^{\text{LS}}$  curves do not overlap in the radiatively dominated region at high carrier concentrations. This difference is further illustrated in Figure 5c, which gives the ratio  $\tau_{\text{film,HLI}}^{\text{LS}}/\tau_{\text{film,HLI}}^{\text{SS}}$  of the two decay times. In the SRH-dominated regime, where recombination depends only linearly on the



charge-carrier concentration  $n$ , the ratio is one, but with higher  $\Delta E_F$  the ratio  $\tau_{\text{film,HLI}}^{\text{LS}}/\tau_{\text{film,HLI}}^{\text{SS}}$  increases toward two as expected from comparison between Equations 4 and 6. In case of Auger recombination being present, the ratio could increase further toward three.

### 2.3. Influence of the Contacts on the Charge-Carrier Decay

At this point we have understood that the decay times resulting from the small-or large-signal approach differ if nonlinear recombination mechanisms are present but should give identical results for lower carrier densities where recombination is dominated by rates  $R(n)$  that are linear in  $n$ . The next step is to consider the complication arising from the presence of contacts to the solar cell which charge up by the extraction of charge carriers. When performing transient measurements of complete solar cells, the charging and discharging of these device electrodes adds an additional effect modifying the shape of the transient decays. Using the simplifications introduced above for the carrier-recombination dynamics, the mathematical problem is still described by an ordinary differential equation in time without any spatial dependences of electron and hole concentrations within the absorber layer. This differential equation (again neglecting Auger recombination) is given by

$$\begin{aligned} \frac{dn(t)}{dt} &= -R(n) + G - \frac{C_{\text{area}}}{qd_{\text{pero}}} \frac{dV_{\text{ext}}(t)}{dt} \\ &= -k_{\text{rad}}n(t)^2 - \frac{n(t)}{\tau_{\text{SRH}}^{\text{eff}}} + G - \frac{C_{\text{area}}}{qd_{\text{pero}}} \frac{dV_{\text{ext}}(t)}{dt} \end{aligned} \quad (8)$$

where  $C_{\text{area}}$  is the area-related capacitance in units of F/cm<sup>2</sup> and  $V_{\text{ext}}$  is the voltage between the electrodes. The differential equation for the small-signal case with bias illumination must again additionally consider the continuous generation rate  $G$  whereas for a large-signal experiment we have  $G = 0$  (see Table S2, Supporting Information). The effect of the term containing the capacitance  $C_{\text{area}}$  in Equation 8 is to consider that charge carriers are transferred from the absorber to the electrodes and vice versa. The loss of carriers from the absorber changes the surface-charge density on cathode and anode until the external voltage  $V_{\text{ext}}$  and the internal quasi-Fermi splitting  $\Delta E_{F,\text{int}} = qV_{\text{int}}$  have equilibrated and no further current is flowing. The amount of charge that needs to be added to or subtracted from the electrodes to accommodate a change in  $V_{\text{ext}}$  is controlled by  $C_{\text{area}}$ . In principle, the internal quasi-Fermi level splitting and the external voltage can have substantially different values during a transient as we can see in Figure 4. But if we focus only on the part of the decay that occurs at longer times and ignore situations with very thick, low conductivity contact layers, the condition  $V_{\text{ext}} \approx V_{\text{int}}$  is a reasonable approximation. Let us further assume that we are in high-level injection ( $n = p$ ) and the electron and hole densities in the absorber scale with voltage as

$$n(t) = p(t) = n_i \exp\left(\frac{qV_{\text{ext}}(t)}{2k_B T}\right) \quad (9)$$

In the following, we derive analytical equations for the large- and small-signal transients, including the three effects of

radiative recombination, SRH recombination and discharging of the contact capacitance. The respective results and solutions for additional situations (e.g., including Auger recombination) are listed in Table S3 (Supporting Information). Because of  $dV_{\text{ext}}/dn = 2k_B T/(qn)$  we rewrite Equation (8) and obtain

$$\begin{aligned} \frac{dn(t)}{dt} &= f(n) = \frac{G - k_{\text{rad}}n(t)^2 - n(t)/\tau_{\text{SRH}}^{\text{eff}}}{1 + \frac{2k_B T/q}{n(t)} \frac{C_{\text{area}}}{qd_{\text{pero}}}} \\ &= \frac{G - k_{\text{rad}}n(t)^2 - n(t)/\tau_{\text{SRH}}^{\text{eff}}}{1 + n_Q/n(t)} \end{aligned} \quad (10)$$

where  $f(n)$  denotes the functional dependence of the total kinetics on  $n$  and  $n_Q = 2C_{\text{area}}k_B T/(q^2 d_{\text{pero}})$  is the charge per volume that is induced on the capacitor by two times the thermal voltage. Thus, in the situation  $n < n_Q$  we would have less charge carriers in the absorber than we have in the contact. In this situation, carrier recombination is considerably delayed through the need to discharge the capacitance before carriers can recombine. For the large-signal decay time we have consequently

$$\tau_{\text{cell,HLI}}^{\text{LS}} = -\frac{n(t)}{dn(t)/dt} = \frac{n_Q/n(t) + 1}{k_{\text{rad}}n(t) + 1/\tau_{\text{SRH}}^{\text{eff}}} \quad (11)$$

where the suffix “cell” in  $\tau_{\text{cell,HLI}}^{\text{LS}}$  symbolizes the inclusion of the capacitance present in complete cells with two electrodes. At high carrier concentrations, the decay time approaches  $\tau_{\text{cell,HLI}}^{\text{LS}}(n \gg 1/(k_{\text{rad}}\tau_{\text{SRH}}^{\text{eff}})) \approx 1/(k_{\text{rad}}n)$ , i.e., the same value as in the case without considering the capacitance. In contrast for low carrier concentrations, the capacitive effect becomes dominant and we have  $\tau_{\text{cell,HLI}}^{\text{LS}}(n \ll n_Q) = n_Q\tau_{\text{SRH}}^{\text{eff}}/n$  leading to long decay times for lower carrier densities  $n(t)$ . Thus, in both limiting cases the decay time is inversely proportional to the carrier density  $n(t)$ .

For the small-signal decay time, we now have to take the derivative  $df/dn$  rather than  $dR/dn$  as we did previously to obtain the result of Equation (6). We obtain

$$\tau_{\text{cell,HLI}}^{\text{SS}} = -\frac{1}{df/dn} = \frac{n_Q/n + 1}{dR/dn} = \frac{n_Q/n + 1}{2k_{\text{rad}}n + 1/\tau_{\text{SRH}}^{\text{eff}}} \quad (12)$$

Like in Equation 11, the decay time  $\tau_{\text{cell,HLI}}^{\text{SS}}$  is delayed by a factor of  $(n_Q/n + 1)$  compared to the decay time  $\tau_{\text{film,HLI}}^{\text{SS}}$  without the capacitive effect. The limiting case for high carrier concentration is given by  $\tau_{\text{cell,HLI}}^{\text{SS}}(n \gg 1/(k_{\text{rad}}\tau_{\text{SRH}}^{\text{eff}})) = 1/(2k_{\text{rad}}n) = \tau_{\text{cell,HLI}}^{\text{LS}}(n \gg 1/k_{\text{rad}}\tau_{\text{SRH}}^{\text{eff}})/2$  and is half the value of the corresponding large-signal decay time. In the case of low carrier concentrations, we have  $\tau_{\text{cell,HLI}}^{\text{SS}}(n \ll n_Q) = n_Q\tau_{\text{SRH}}^{\text{eff}}/n = \tau_{\text{cell,HLI}}^{\text{LS}}(n \ll n_Q)$ , i.e., there is no difference between large- and small signal decay times.

It is important to notice that in both limiting cases, large- and small-signal decay time are inversely proportional to the carrier density and do not carry direct information on the effective carrier lifetime  $\tau_{\text{SRH}}^{\text{eff}}$ . However, an intermediate concentration range where  $n_Q < n < 1/k_{\text{rad}}\tau_{\text{SRH}}^{\text{eff}}$ , if existing, provides a parameter window for the access to this quantity. Since the inflection points (ip) of the double logarithmic curves  $\tau_{\text{cell,HLI}}^{\text{LS}}(n)$  and  $\tau_{\text{cell,HLI}}^{\text{SS}}(n)$  are given by  $\tau_{\text{cell,HLI}}^{\text{SS}}(n_{\text{ip}}^{\text{SS}} = \sqrt{n_Q/2k_{\text{rad}}\tau_{\text{SRH}}^{\text{eff}}}) = \tau_{\text{SRH}}^{\text{eff}}$  and  $\tau_{\text{cell}}^{\text{LS}}(n_{\text{ip}}^{\text{LS}} = \sqrt{n_Q/k_{\text{rad}}\tau_{\text{SRH}}^{\text{eff}}}) = \tau_{\text{SRH}}^{\text{eff}}$ , a fit of Equations (11)

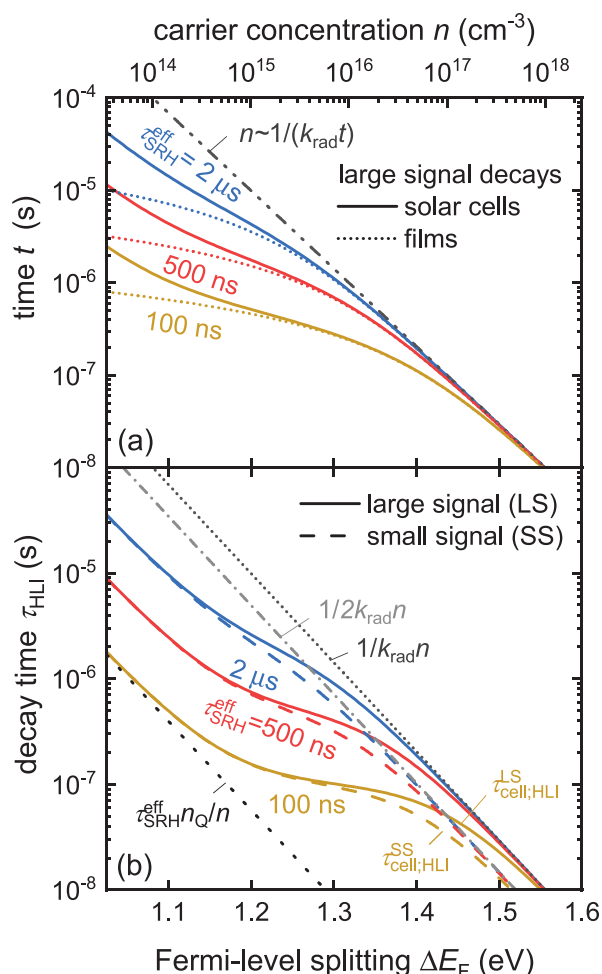


**Figure 6.** a) Transients  $n(t)$  calculated from the explicit solution (Table S2, Supporting Information) for the differential equation in Equation (10) (large-signal case  $G = 0$ ) representing recombination that is further delayed by capacitive charging of the junction, typically measured on completed solar cells (solid lines). Parameters are given in Table 2. Including the junction charging leads to a slowing down of all three transients in the range  $n < n_Q$  as compared to the transients without junction charging (dotted lines, see also Figure 5a). b) Comparison of large-signal decay times  $\tau_{\text{cell,HLI}}^{\text{LS}}$  (full lines) and the small-signal decay times  $\tau_{\text{cell,HLI}}^{\text{SS}}$  (dashed lines) as a function of  $\Delta E_F$  (lower axis) and  $n$  (upper axis) following the implicit Equations (11) and (12) for the large- and the small-signal case, respectively. At high carrier concentrations the decay times follow the asymptotes given by the quadratic radiative recombination term. At low concentrations ( $n < n_Q$ ) both decay times are dominated by the capacitive delay following  $\tau_{\text{cell,HLI}}^{\text{LS}} \approx \tau_{\text{cell,HLI}}^{\text{SS}} \approx \tau_{\text{SRH}}^{\text{eff}} n_Q / n$ . The transition between these two asymptotic cases occurs in the range of decay times  $\tau_{\text{cell,HLI}}^{\text{LS}} \approx \tau_{\text{SRH}}^{\text{eff}}$ .

and (12) to experimental data may provide an estimate of  $\tau_{\text{SRH}}^{\text{eff}}$ ,  $n_Q$ , and  $k_{\text{rad}}$  (see Section S2, Supporting Information). Furthermore, the information on  $\tau_{\text{SRH}}^{\text{eff}}$  is available even without knowledge of the absolute values of  $n$ .

Figure 6a compares the explicit solutions for the large-signal transients (full lines) including the capacitive charging to those without this effect (dashed lines, same data as in Figure 5a). For small times, i.e., high carrier concentrations, all transients are dominated by radiative recombination, whereas after longer

times, at lower carrier concentrations, the slowing down of the transients by capacitive discharge is clearly visible. This effect is also seen in the large- and small-signal decay times  $\tau_{\text{cell,HLI}}^{\text{LS}}$  and  $\tau_{\text{cell,HLI}}^{\text{SS}}$  given by Equations (11) and (12) and shown in Figure 6b. Notably, toward low carrier densities all curves exhibit an asymptotic behavior  $\tau_{\text{cell,HLI}}^{\text{LS}} \approx \tau_{\text{cell,HLI}}^{\text{SS}} \approx \tau_{\text{SRH}}^{\text{eff}} n_Q / n$  resulting from the capacitive discharge of charge carriers from the junction with subsequent recombination. In this regime, there is no difference between the large- and the small-signal decay time, whereas at high carrier densities we have the asymptotes  $\tau_{\text{cell,HLI}}^{\text{LS}} \approx 1/(k_{\text{rad}} n)$  and  $\tau_{\text{cell,HLI}}^{\text{SS}} \approx 1/(2k_{\text{rad}} n)$  determined by radiative recombination. Between these two limiting regimes there exists a window of voltages or carrier densities (around the inflection point of the curves) that allows the determination of the effective SRH lifetime  $\tau_{\text{SRH}}^{\text{eff}}$ . Figure 6b demonstrates also that the width of this window depends on the actual value of  $\tau_{\text{SRH}}^{\text{eff}}$ , becoming narrower the more  $\tau_{\text{SRH}}^{\text{eff}}$  approaches  $1/(k_{\text{rad}} n_Q)$ .

#### 2.4. Influence of the Mode of Detection on the Decay Times

So far, we have discussed the general differences between small-signal and large-signal methods as well as between samples that contain a single semiconductor layer as opposed to complete devices that contain a nonzero capacitance due to their electrodes. The remaining difference between TPL and TPV measurements are the mode of detection and the way how we derive the decay times from the respective observables  $\phi_{\text{TPL}}(t)$  and  $\Delta V_{\text{oc}}(t)$ . In case of TPL, the detected photon flux  $\phi_{\text{TPL}}(t)$  under HLI conditions will be proportional to  $n^2$  and hence we define the TPL decay time  $\tau_{\text{TPL,HLI}}^{\text{LS}}$  via<sup>[48]</sup>

$$\tau_{\text{TPL,HLI}}^{\text{LS}} = \left( -\frac{1}{2} \frac{d \ln(\phi_{\text{TPL}})}{dt} \right)^{-1} = \left( -\frac{d \ln(n)}{dt} \right)^{-1} \quad (13)$$

Note that the factor 1/2 in the second term of Equation 13 adjusts  $\tau_{\text{TPL,HLI}}^{\text{LS}}$  to the large-signal decay time  $\tau_{\text{film,HLI}}^{\text{LS}}$  or  $\tau_{\text{cell,HLI}}^{\text{LS}}$  of the carrier concentration under high-level injection (HLI) conditions.

In case of TPV, the excess-open circuit voltage  $\Delta V_{\text{oc}}$  is used to detect the excess-carrier density. Again, under high-level injection, we have

$$\begin{aligned} \Delta V_{\text{oc}} &= \frac{k_B T}{q} \ln \left( \frac{n^2}{n_i^2} \right) - \frac{k_B T}{q} \ln \left( \frac{n_{\text{bias}}^2}{n_i^2} \right) = 2 \frac{k_B T}{q} \ln \left( \frac{n}{n_{\text{bias}}} \right) \\ &= 2 \frac{k_B T}{q} \ln \left( 1 + \frac{\Delta n_{\text{laser}}}{n_{\text{bias}}} \right) \end{aligned} \quad (14)$$

where  $n_i$  is the intrinsic charge-carrier concentration,  $k_B T/q$  the thermal voltage and  $n = n_{\text{bias}} + \Delta n_{\text{laser}}$  is the carrier density during the transient experiment that can be split up into the steady state bias charge-carrier density  $n_{\text{bias}}$  and the excess-charge density  $\Delta n_{\text{laser}}$  that is induced by the laser pulse. The typically used approach in literature<sup>[77]</sup> is now to assume that  $dV_{\text{oc}}/dt \propto d\Delta n_{\text{laser}}/dt$  holds if the excess voltage is sufficiently small. This approach has previously been shown by Wood

et al.<sup>[78]</sup> to cause errors in determining the correct decay time of the carrier density. Let us briefly discuss the assumption  $d\Delta V_{oc}/dt \propto d\Delta n_{laser}/dt$  critically. If we assume that  $\Delta n_{laser}$  decays exponentially, we might expect that also  $\Delta V_{oc}$  decays exponentially with the same time constant  $\tau$ . However, if we insert  $\Delta n_{laser}(t) = \Delta n_{max} \exp(-t/\tau)$  into Equation (14), we obtain a decay that is not monoexponential and a decay time that is given by

$$\tau_{TPV,HLI}^{ss} = -\frac{dt}{d \ln(\Delta V_{oc})} = \tau \left\{ 1 + \frac{1}{\gamma} \exp\left(\frac{t}{\tau}\right) \right\} \ln \left\{ 1 + \gamma \exp\left(-\frac{t}{\tau}\right) \right\} \quad (15)$$

where we use the definition  $\gamma = \Delta n_{max}/n_{bias}$ . Note that  $\tau_{TPV,HLI}^{ss}$  is still a function of time and not a constant. Only for long times  $t \gg \tau$  and/or small values of  $\gamma$ , Equation 15 approaches  $\tau_{TPV,HLI}^{ss} = \tau$ . As shown in the Figure S3 (Supporting Information), for realistic values of  $\gamma$  there can be differences between the decay times  $\tau_{TPV}^{ss}$  and  $\tau$  of  $\Delta V_{oc}$  and  $\Delta n$ . These differences can be on the order of factor 2 or less. Thus, they could not explain the large discrepancies shown in Figure 1 but they could affect comparisons between samples that may have similar TPV decay times at a given voltage but where the condition of equal voltage perturbation  $\Delta V_{oc}$  is not fulfilled.

### 3. Experimental Results

Finally, we want to apply and transfer our findings to experimental data and unify the information contained in transient photoluminescence and transient photovoltage data. Therefore, we performed TPL and TPV measurements on the same solar cell (glass/ITO/PTAA/MAPI/PCBM/BCP/Ag) using the setup illustrated in Figure 2. The investigated solution-processed MAPI solar cell has already been introduced previously<sup>[49]</sup> and has a very high open-circuit voltage of 1.25 V. The TPV data is compared to previously published TPL data of the same solar cell and of a perovskite film on glass,<sup>[49]</sup> which was passivated with the molecule n-trioctylphosphine oxide (TOPO) that strongly reduces surface recombination velocities (layer stack is therefore glass/MAPI/TOPO).<sup>[39]</sup>

Figure 7 shows the small-signal decay times  $\tau_{TPV,HLI}^{ss}$  (blue stars) as a function of the open-circuit voltage, which are extracted by fitting the TPV transients recorded at different bias light intensities using Equation 1, and the large-signal decay time  $\tau_{TPL,HLI}^{ls}$  (red and grey spheres) versus the quasi-Fermi-level splitting ( $\Delta E_F$ ) derived from TPL by taking the derivative of the PL at each time using Equation (13). The respective transient decays were already shown in Figure 3a,b. The TPL data is recorded with a gated CCD camera that works by using and amplifying only that part of the signal that corresponds to a certain delay time after the laser pulse. This amplification (gain) can be changed but the overall signal strength (number of counts) must not exceed a certain value to avoid any damage to the detector. In order to improve the dynamic range, we therefore adjusted the gain settings and integration times for different parts of the decay. Low gains and integration times were used for short delay times, where the luminescence is still high, while higher gains and integration times were used for longer delay times, where the signal would otherwise be already close to the noise level. Thereby, we could improve the dynamic range

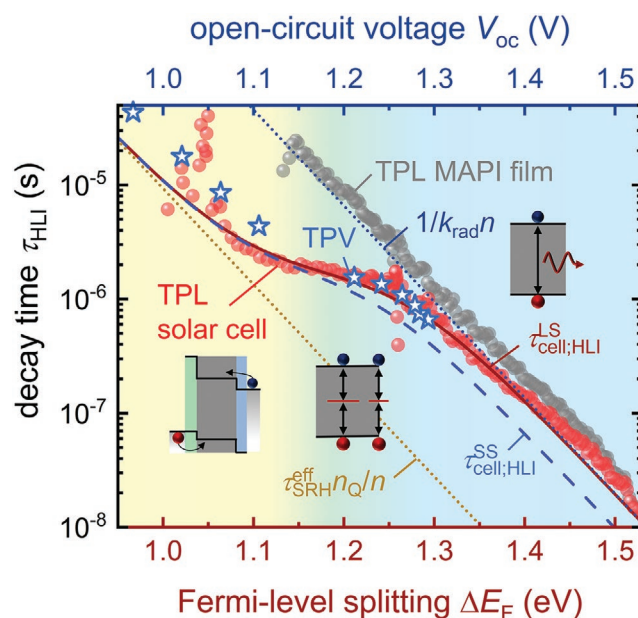


**Figure 7.** Experimental data of the decay time derived from large-signal TPL measurements ( $\tau_{TPL,HLI}^{ls}$ ) of a perovskite film (grey spheres) and the solar cell (red spheres) (data from ref. [49]) and TPV measurements ( $\tau_{TPV,HLI}^{ss}$ ) at different bias illumination intensities (blue stars). Furthermore, the exponential slope of the capacitance-dominated (light yellow) and the radiatively dominated (light blue) regions are shown as guide to the eye. Furthermore, we added the results of our analytical model (see Equations 11 and 12) for small- (blue dashed line) and large-signal (red solid line) transients on cells. The parameters used for the analytical solutions are stated in Table 3.

of the TPL data to around 7 to 8 orders of magnitude which is crucial to cover all three regions of the decay (radiative, SRH and capacitive). The different TPL datasets were then combined to one dataset, which was smoothed before we applied Equation (13) to obtain the decay times over a voltage range from around 1.1 eV to around 1.55 eV. About  $60mV \approx kT/q \ln(10)$  on the x-axis of Figure 7 correspond to one order of magnitude of PL intensity. Note that the part of the data that originates from PL decay times below around 1.1eV is the part of the data that corresponds to the PL decay approaching the noise level at long delay times. Here, the decay times look particularly noisy. This is due to the fact that the procedure of taking the derivative of (in this part of the curve) noisy raw data amplifies the noise even further. Therefore, this part of decay time data should not be considered to be overly trustworthy.

For the solar cell, the experimentally determined decay times  $\tau_{TPL,HLI}^{ls}$  from TPL and  $\tau_{TPV,HLI}^{ss}$  from TPV show the typical shape (three regions) already known from the analytical solutions and derived in the last section (see Figure 6b). The large-signal decay time  $\tau_{TPL,HLI}^{ls}$  for the passivated film on glass (grey) is dominated by radiative recombination over the complete range of quasi-Fermi-level splitting, which was experimentally accessible, and increases continuously for smaller  $\Delta E_F$ . This behavior implies that SRH lifetimes have to be extremely long (at least 40  $\mu s$ ) as previously observed in refs. [79] for samples of this type.<sup>[49]</sup> This leads to the situation that if only one decay time constant is reported, the result would strongly depend on the laser fluence

**Table 3.** Parameters used for Figure 7.

Parameter	Unit	Value(s)
SRH lifetime $\tau_{\text{SRH}}^{\text{eff}}$	$\mu\text{s}$	1.7
Radiative recombination coefficient $k_{\text{rad}}$	$\text{cm}^3 \text{s}^{-1}$	$1.5 \times 10^{-10}$
Capacitance per area $C_{\text{area}}$	$\text{nF cm}^{-2}$	10
thickness	Nm	280
Intrinsic carrier concentration $n_i$	$\text{cm}^{-3}$	$8.05 \times 10^4$

and excitation density at which the data is evaluated with decay times  $\tau_{\text{TPV,HLI}}^{\text{LS}}$  varying from tens of ns to tens of  $\mu\text{s}$  within our experimentally accessible range (see grey data points in Figure 7). Note that for the highest values of  $\Delta E_{\text{F}}$ , also Auger recombination might contribute to the decay time. This result highlights the importance of comparing data at equal charge-carrier density or quasi-Fermi level splitting<sup>[80]</sup> and to identify—e.g., from differential decay time versus quasi-Fermi level splitting plots—whether the decay in a certain range is consistent with radiative or with some type of SRH recombination. In this context, the radiatively dominated region (light blue) can be identified by the exponential slope being proportional to  $\propto \exp(-\Delta E_{\text{F}}/(2k_{\text{B}}T))$ . The part of the data showing the smallest slope of decay time with  $\Delta E_{\text{F}}$  (light green) is indicative of recombination that is approximately linear in electron and hole density, which should be SRH recombination in the bulk and at interfaces.

In addition to the experimental data, we also added solutions to the analytical Equations 11 and 12 for  $\tau_{\text{cell,HLI}}^{\text{SS}}$  (blue dashed line) and  $\tau_{\text{cell,HLI}}^{\text{LS}}$  (red solid line) using the parameters given in Table 3. We used the same value for  $k_{\text{rad}}$  as done previously in ref. [49] to numerically fit the TPL data using TCAD Sentaurus. The other parameters are chosen such that the red solid line well reproduces the red symbols, i.e., the TPL data of the cell. We note that this approach leads to some discrepancies in explaining the TPV data (blue stars) with the solution of Equation (12) (blue dashed line). A range of reasons are likely to contribute to this discrepancy. First of all, we assume that we can neglect any gradients of quasi-Fermi level over the transport layers during the later parts of the TPV and TPL transients such that Equation (9) is a good approximation to reality. Furthermore, the differential equations assume that  $n = p$  in the absorber, which can easily be violated even in the absence of doping if injection and extraction of holes is slightly different from that of electrons. Also, asymmetric capture coefficients of defects could lead to unequal electron and hole densities. In addition, while we perform a differential analysis of the large-signal decay, the small signal TPV decay is typically analyzed by a monoexponential fit even though the data will not be entirely monoexponential. Therefore, also the exact mode of fitting can lead to variations in the extracted decay times. Finally, the deviations may be at least in part a consequence of the fact that the TPV data is never determined in true small-signal conditions as discussed in Section 2.4. Thus, the experimental TPV data may indeed be always slightly higher than where the TPV data would be expected to be based on Equation (12), which assumes an infinitely small voltage perturbation by the laser pulse on top of the bias light. In our data, this leads to the consequence that the blue stars are nearly overlapping with the red spheres at the onset of the radiative region (1.25 to 1.3 V) rather than being offset by a

factor of 2 (as is the case for the blue dashed line relative to the red solid line).

The experimental data in Figure 7 also explains the large discrepancies between TPV and TPL lifetimes stated in the literature on halide perovskites, where the decay time from TPV is often much longer than the one extracted from TPL. These long TPV decay times result from the slow capacitive charging and discharging effects occurring in samples with a significant electrode capacitance as previously observed by Kiermasch et al.<sup>[1]</sup> or Wang et al.<sup>[43]</sup> This discharging process superimposes recombination and dominates the small-signal decay time signal  $\tau_{\text{TPV,HLI}}^{\text{SS}}$  at small Fermi-level splitting (light yellow region). Since typically low bias-light intensities are used for TPV, not exceeding several suns, open-circuit voltages at which TPV is recorded are low, thus the data points lie in this capacitively dominated region of the decay time versus  $\Delta E_{\text{F}}$  or  $V_{\text{oc}}$  graph. It requires very high bias-light intensities or, as in our example, solar cells with a very high open-circuit voltage at one sun illumination (1.25 V), to see more than just capacitive discharging effects in the TPV signal. Note that the exponential slope in the decay time versus or  $V_{\text{oc}}$  curve caused by the capacitive discharge of the electrodes and the radiative recombination are equal ( $\propto \exp(-\Delta E_{\text{F}}/(2k_{\text{B}}T))$ ).

## 4. Numerical Simulations

With the exception of Figure 4, we used so far ordinary differential equations in time to understand how decay times in pulsed experiments depend on carrier density, sample type and small- versus large-signal excitation. However, the downside of this approach is that we have to make a whole range of assumptions as pointed out in Table 1. For instance, we had to neglect all spatial dependences of carrier densities. While we could distinguish between charge carriers in the absorber and charge on the electrodes, we did not include a realistic model of charge transport inside the perovskite and through the electron- and hole transport layers. Therefore, we performed numerical simulations using Sentaurus TCAD that solve coupled partial differential equations in time and space for electrons, holes and space charge (Poisson equation). Transient device simulations were conducted for the TPL situation using a laser fluences of  $10 \mu\text{J cm}^{-2}$  and at different bias illumination intensities ranging from 0.01-1000 suns and an adjusted laser fluence to simulate the small-signal TPV transients. In Figure 8a, a comparison of the resulting small- and the large-signal decay times as a function of the internal (TPL) or external (TPV) Fermi-level splitting is illustrated for varying SRH bulk lifetimes ranging from 100 ns to 20  $\mu\text{s}$ . In this example, the interfaces between the perovskite absorber and the charge-extracting layers are nearly ideal (low  $S$ , no or small band offsets) and similar to the simulation parameters used in Figure 4 (see Table S5, Supporting Information). The fundamental difference between the small- and large-signal decay times at high Fermi-level splitting is also visible here, which leads to the small-signal decay times being always smaller by a factor of two. Contrary to the analytical results presented in Figure 6, the small- and the large-signal decay times are also not the same at lower Fermi-level-splitting, where SRH bulk recombination or capacitive discharging



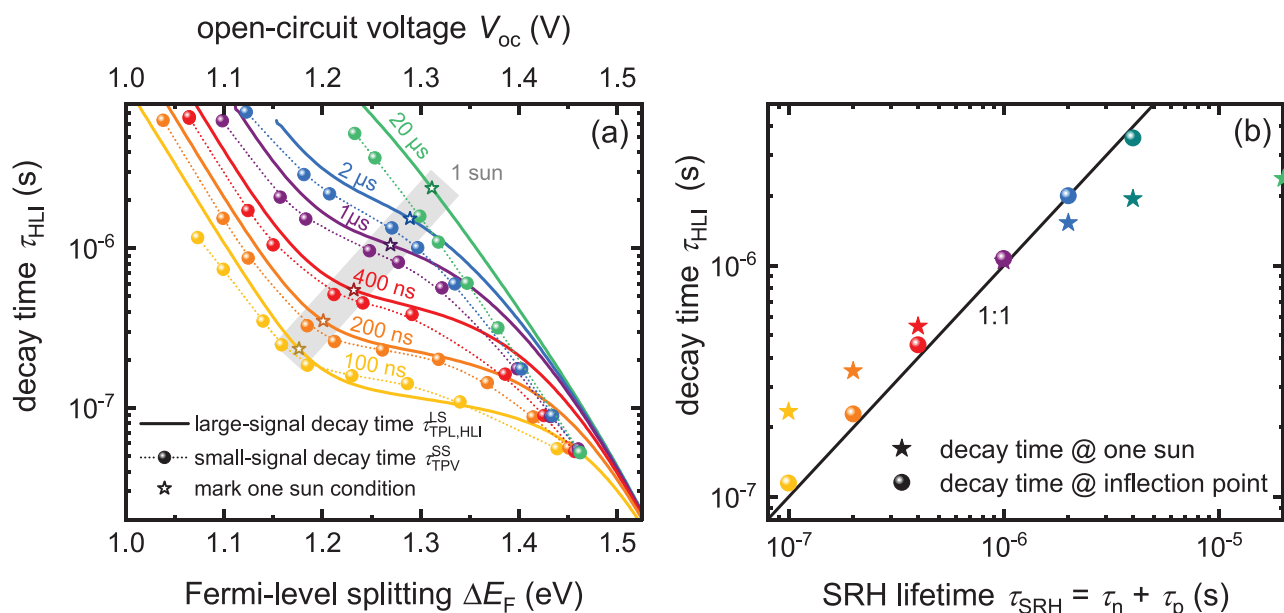


**Figure 8.** a) Decay times versus Fermi-level splitting or open-circuit voltage resulting from numerical simulations of TPL and TPV on a solar cell stack using Sentaurus TCAD for various SRH bulk lifetimes. The simulated solar cell devices are characterized by slow interface recombination velocities ( $S = 0.01 \text{ cm s}^{-1}$ ) at both absorber-transport layer interfaces, while the SRH bulk lifetime is varied from 100 ns (yellow) to 20  $\mu$ s (green). The lines represent the large-signal decay time derived by taking the derivative of the PL at each time (see Equation 5). The data points belong to the simulation of transient photovoltage for different bias light intensities and result from the analysis of the small perturbation voltage decay. The stars mark the respective open-circuit voltage at one sun. b) Decay times taken from (a) at the inflection point of the large-signal curves (spheres) compared to the points taken at one sun (stars) compared to the SRH lifetime that was used as input to the Sentaurus simulations.

dominates. The reason for this is that the concentration of electrons and holes is neither identical nor constant as a function of position in the Sentaurus TCAD simulations (see band diagrams in Figure 4). Therefore, the solar cell is no longer exactly in high-level injection ( $n = p$ ), which is a necessary simplification to get the analytical solutions illustrated in Figure 6 and listed in Table S2 (Supporting Information).

Figure 8b illustrates the different ways of comparing decay times. Here we compare two options, namely using the large-signal decay time at one sun or using the large-signal decay time at the inflection point of the decay time versus  $\Delta E_F$  plot. We find that in line with our expectations (see Section 2, Supporting Information), the decay time at the inflection point (spheres) reproduces the actual SRH lifetime (black line) reasonably well while the decay time at one sun differs from the SRH lifetime except at one point that is—in this example—at around 1  $\mu$ s. Here, the inflection point is approximately at one sun and both values are approximately identical to  $\tau_{SRH}$ . Note that above an SRH lifetime of 4  $\mu$ s, there is no inflection point anymore that could be evaluated and the radiative and capacitive branches of the decay time become indistinguishable.

## 5. Discussion and Outlook

For most state-of-the-art publications on halide-perovskite solar cells, quantifying recombination is a near-mandatory exercise. Often, transient methods are used to show how the voltage, charge-carrier density or luminescence decay after a laser pulse. However, the measured reported decay times may vary by orders

of magnitude from sample to sample but more importantly also from method to method. In particular, methods based on electrical detection (such as TPV or open-circuit voltage decay) often result in much longer time constants as compared to purely optical methods measured on thin films from the same material (as shown in Figure 1), calling in question the physical meaning of the measured decay times. The large method-specific variation in time constants is partly caused by a substantial dependence of the decay time on the actual charge-carrier density in the absorber (or the voltage at the terminals of the device) as shown in the present analysis. Thus, measured decay times without reference to the actual carrier concentration or bias voltage under which these values are obtained are essentially worthless. In a complete solar cell, essentially arbitrarily large “lifetimes” can be measured with an electrical technique like TPV if the bias condition is sufficiently low and the cell is not shunted. This is true even if the actual SRH lifetime was fairly low.

In perovskite-solar cells several recombination mechanisms as well as carrier extraction and injection affect the charge-carrier density in the absorber layer. These mechanisms have a different dependence of their rate on charge-carrier density with the following consequences: i) deviations from monoexponential decays in large-signal measurements and ii) a bias dependence of the decay time in small-signal TPV experiments. In the present approach, we distinguish three regimes of working conditions: 1) At high charge-carrier densities, higher-order recombination processes such as Auger and radiative recombination dominate leading to fast decay times. 2) At intermediate charge densities, defect-assisted recombination at the bulk or interface determines the decay. 3) At low charge-carrier densities



re-injection of charge carriers from the electrodes into the absorber leads to a slow decay whose decay time varies exponentially with Fermi-level splitting ( $\tau \propto \exp(-\Delta E_F/(2k_B T))$ ). The first two mechanisms are present both in films and devices while the last mechanism requires the presence of electrodes and is therefore only observed in finished devices.

In order to better compare optical and electrical measurements of decay times, these different regimes have to be distinguished and therefore the decay times have to be investigated over a wide range of carrier densities and/or voltages. Displaying decay times as a function of voltage or carrier density is common practice, e.g., for TPV data in organic photovoltaics<sup>[81]</sup> or for photoconductance decay data of Si wafers.<sup>[82]</sup> However, for halide-perovskite films or devices charge-carrier-density dependent data is only infrequently shown leaving ample room for misinterpretations. The present results demonstrate that displaying large- and small-signal decay times over the voltage or the Fermi-level splitting as a common representation of injection level is mandatory. Note that for changing the injection level, we require many measurements at different bias level for TPV (small signal) but only one measurement for TPL that is however analyzed differentially by applying Equation 13.

We have shown that even the most generic model of a solar cell, including only radiative and nonradiative SRH recombination combined with a capacitor that builds up the electrostatic potential of the solar cell, predicts decay times measured by large- and small-signal transients to vary over many orders of magnitudes. Only if the experimental data cover the relevant regimes of carrier concentrations, analysis of these data by the implicit solutions to the differential equations (see Equations 11 and 12), allows us to derive valuable information like the capacitance  $C_{\text{area}}$ , the effective radiative coefficient  $k_{\text{rad}}$ , and the effective SRH lifetime  $\tau_{\text{eff}}^{\text{SRH}}$ . Especially information on the latter quantity is important when studying the influence of contact recombination on the nonradiative limitations of perovskite solar cells, by comparing lifetimes measured during different stages of device fabrication.

It is important to note that the analysis of experimental data with the present simple, generic model is not necessarily possible for all types of perovskite solar cells. While we found agreement for our high open-circuit voltage cells, previously published TPL data on coevaporated cells shows deviations from the predicted behavior that are consistent with numerical models but not with our simple analytical models.<sup>[49]</sup> Here we have to remember the approximations made in using ordinary differential equations in time and not in space (see Table 1). These equations therefore neglect a possible difference between the internal split of quasi-Fermi-levels and the externally measured voltage.<sup>[83,84]</sup> They assume a simple high-level injection recombination mechanism with ideality factor  $n_{\text{id}} = 2$  for the part of the recombination that is limited by SRH recombination superimposed with radiative recombination with  $n_{\text{id}} = 1$  toward higher injection conditions<sup>[69,85]</sup> while it disregards shallow defects that cannot be described by a simple SRH lifetime. All these effects may lead to deviations from the observation of three distinct and discernible regimes which will necessitate the use of numerical models for data interpretation as we have shown in Figures 4 and 8.

## Supporting Information

Supporting Information is available from the Wiley Online Library or from the author.

## Acknowledgements

The authors acknowledge support from the Helmholtz Association via the project PEROSEED and via the project-oriented funding (POF IV).

Open access funding enabled and organized by Projekt DEAL.

## Conflict of Interest

The authors declare no conflict of interest.

## Author contributions

L.K., U.R., and T.K. developed the overall concept of the paper. L.K., T.K., and U.R. prepared the manuscript. L.K. performed the simulations. L.K., T.K., and U.R. handled the mathematics to derive the analytical solutions and analyzed the experimental data. B.K. developed the basis of the Sentaurus TCAD code, which was modified by L.K. Z.L. fabricated the solar cell devices. L.K. performed the tr-PL and TPV measurements. All authors discussed the results and commented on the manuscript.

## Data Availability Statement

The data that support the findings of this study are available from the corresponding author upon reasonable request.

## Keywords

capacitive discharge, charge-carrier lifetime, decay time, photovoltaics, time-resolved photoluminescence

Received: July 27, 2021

Revised: September 19, 2021

Published online: October 23, 2021

- [1] D. Kiermasch, A. Baumann, M. Fischer, V. Dyakonov, K. Tvingstedt, *Energy Environ. Sci.* **2018**, *11*, 629.
- [2] I. Levine, A. Al-Ashouri, A. Musiienko, H. Hempel, A. Magomedov, A. Dreivilkauskaitė, V. Getautis, D. Menzel, K. Hinrichs, T. Unold, S. Albrecht, T. Dittrich, *Joule* **2021**, <https://doi.org/10.1016/j.joule.2021.07.016>.
- [3] S. Wheeler, D. Bryant, J. Troughton, T. Kirchartz, T. Watson, J. Nelson, J. R. Durrant, *J. Phys. Chem. C* **2017**, *121*, 13496.
- [4] R. K. Ahrenkiel, *Solid-State Electron.* **1992**, *35*, 239.
- [5] M. Maiberg, R. Scheer, *J. Appl. Phys.* **2014**, *116*, 123711.
- [6] E. M. Hutter, J. J. Hofman, M. L. Petrus, M. Moes, R. D. Abellón, P. Docampo, T. J. Savenije, *Adv. Energy Mater.* **2017**, *7*, 1602349.
- [7] E. M. Hutter, G. E. Eperon, S. D. Stranks, T. J. Savenije, *J. Phys. Chem. Lett.* **2015**, *6*, 3082.
- [8] E. M. Hutter, R. J. Sutton, S. Chandrashekar, M. Abdi-Jalebi, S. D. Stranks, H. J. Snaith, T. J. Savenije, *ACS Energy Lett.* **2017**, *2*, 1901.
- [9] Y. Yamada, T. Nakamura, M. Endo, A. Wakamiya, Y. Kanemitsu, *J. Am. Chem. Soc.* **2014**, *136*, 11610.

- [10] J. M. Richter, M. Abdi-Jalebi, A. Sadhanala, M. Tabachnyk, J. P. H. Rivett, L. M. Pazos-Outón, K. C. Gödel, M. Price, F. Deschler, R. H. Friend, *Nat. Commun.* **2016**, 7, 13941.
- [11] T. Du, W. Xu, S. Xu, S. R. Ratnasingham, C.-T. Lin, J. Kim, J. Briscoe, M. A. McLachlan, J. R. Durrant, *J. Mater. Chem. C* **2020**, 8, 12648.
- [12] A. Paulke, S. D. Stranks, J. Kniepert, J. Kurpiers, C. M. Wolff, N. Schön, H. J. Snaith, T. J. K. Brenner, D. Neher, *Appl. Phys. Lett.* **2016**, 108, 113505.
- [13] M. Petrović, T. Ye, C. Vijila, S. Ramakrishna, *Adv. Energy Mater.* **2017**, 7, 1602610.
- [14] C. G. Shuttle, B. O'Regan, A. M. Ballantyne, J. Nelson, D. D. C. Bradley, J. de Mello, J. R. Durrant, *Appl. Phys. Lett.* **2008**, 92, 093311.
- [15] T. Offermans, S. C. J. Meskers, R. A. J. Janssen, *J. Appl. Phys.* **2006**, 100, 074509.
- [16] J. Bisquert, M. Janssen, *J. Phys. Chem. Lett.* **2021**, 12, 7964.
- [17] S. Ravishanker, A. Riquelme, S. K. Sarkar, M. Garcia-Battle, G. Garcia-Belmonte, J. Bisquert, *J. Phys. Chem. C* **2019**, 123, 24995.
- [18] A. O. Alvarez, S. Ravishanker, F. Fabregat-Santiago, *Small Methods* **2021**, 5, 2100661.
- [19] T. Unold, L. Güta, *Photoluminescence Analysis of Thin-Film Solar Cells*, Wiley-VCH, Weinheim **2016**, p. 275.
- [20] Q. Chen, H. Zhou, Y. Fang, A. Z. Stieg, T.-B. Song, H.-H. Wang, X. Xu, Y. Liu, S. Lu, J. You, *Nat. Commun.* **2015**, 6, 7269.
- [21] B. Chen, S.-W. Baek, Y. Hou, E. Aydin, M. De Bastiani, B. Scheffel, A. Proppe, Z. Huang, M. Wei, Y.-K. Wang, E.-H. Jung, T. G. Allen, E. Van Kerschaver, F. P. G. de Arquer, M. I. Saidaminov, S. Hoogland, S. De Wolf, E. H. Sargent, *Nat. Commun.* **2020**, 11, 1257.
- [22] Y. Li, Y. Zhao, Q. Chen, Y. Yang, Y. Liu, Z. Hong, Z. Liu, Y.-T. Hsieh, L. Meng, Y. Li, *J. Am. Chem. Soc.* **2015**, 137, 15540.
- [23] Q. Jiang, Y. Zhao, X. Zhang, X. Yang, Y. Chen, Z. Chu, Q. Ye, X. Li, Z. Yin, J. You, *Nat. Photonics* **2019**, 13, 460.
- [24] H. Tan, A. Jain, O. Voznyy, X. Lan, F. P. G. De Arquer, J. Z. Fan, R. Quintero-Bermudez, M. Yuan, B. Zhang, Y. Zhao, *Science* **2017**, 355, 722.
- [25] H.-H. Wang, Q. Chen, H. Zhou, L. Song, Z. St Louis, N. De Marco, Y. Fang, P. Sun, T.-B. Song, H. Chen, *J. Mater. Chem. A* **2015**, 3, 9108.
- [26] R. Wang, J. Xue, L. Meng, J.-W. Lee, Z. Zhao, P. Sun, L. Cai, T. Huang, Z. Wang, Z.-K. Wang, *Joule* **2019**, 3, 1464.
- [27] R. Wang, J. Xue, K.-L. Wang, Z.-K. Wang, Y. Luo, D. Fenning, G. Xu, S. Nuryeva, T. Huang, Y. Zhao, J. L. Yang, J. Zhu, M. Wang, S. Tan, I. Yavuz, K. N. Houk, Y. Yang, *Science* **2019**, 366, 1509.
- [28] S. Yang, S. Chen, E. Mosconi, Y. Fang, X. Xiao, C. Wang, Y. Zhou, Z. Yu, J. Zhao, Y. Gao, *Science* **2019**, 365, 473.
- [29] X. Zheng, B. Chen, J. Dai, Y. Fang, Y. Bai, Y. Lin, H. Wei, X. C. Zeng, J. Huang, *Nat. Energy* **2017**, 2, 17102.
- [30] H. Zhou, Q. Chen, G. Li, S. Luo, T.-b. Song, H.-S. Duan, Z. Hong, J. You, Y. Liu, Y. Yang, *Science* **2014**, 345, 542.
- [31] H. Back, G. Kim, H. Kim, C.-Y. Nam, J. Kim, Y. R. Kim, T. Kim, B. Park, J. R. Durrant, K. Lee, *Energy Environ. Sci.* **2020**, 13, 840.
- [32] T. Du, J. Kim, J. Ngiam, S. Xu, P. R. F. Barnes, J. R. Durrant, M. A. McLachlan, *Adv. Funct. Mater.* **2018**, 28, 1801808.
- [33] J. Tian, J. Wang, Q. Xue, T. Niu, L. Yan, Z. Zhu, N. Li, C. J. Brabec, H. L. Yip, Y. Cao, *Adv. Funct. Mater.* **2020**, 30, 2001764.
- [34] F. Tan, H. Tan, M. I. Saidaminov, M. Wei, M. Liu, A. Mei, P. Li, B. Zhang, C.-S. Tan, G. Gong, Y. Zhao, A. R. Kirmani, Z. Huang, J. Z. Fan, R. Quintero-Bermudez, J. Kim, Y. Zhao, O. Voznyy, Y. Gao, F. Zhang, L. J. Richter, Z.-H. Lu, W. Zhang, E. H. Sargent, *Adv. Mater.* **2019**, 31, 1807435.
- [35] J. Wang, J. Zhang, Y. Zhou, H. Liu, Q. Xue, X. Li, C.-C. Chueh, H.-L. Yip, Z. Zhu, A. K. Jen, *Nat. Commun.* **2020**, 11, 177.
- [36] K. Xiao, R. Lin, Q. Han, Y. Hou, Z. Qin, H. T. Nguyen, J. Wen, M. Wei, V. Yeddu, M. I. Saidaminov, Y. Gao, X. Luo, Y. Wang, H. Gao, C. Zhang, J. Xu, J. Zhu, E. H. Sargent, H. Tan, *Nat. Energy* **2020**, 5, 870.
- [37] S. Yang, J. Dai, Z. Yu, Y. Shao, Y. Zhou, X. Xiao, X. C. Zeng, J. Huang, *J. Am. Chem. Soc.* **2019**, 141, 5781.
- [38] Q. Yao, Q. Xue, Z. Li, K. Zhang, T. Zhang, N. Li, S. Yang, C. J. Brabec, H.-L. Yip, Y. Cao, *Adv. Mater.* **2020**, 32, 2000571.
- [39] D. W. deQuilettes, S. Koch, S. Burke, R. K. Paranjy, A. J. Shropshire, M. E. Ziffer, D. S. Ginger, *ACS Energy Lett.* **2016**, 1, 438.
- [40] S. Jariwala, S. Burke, S. Dunfield, R. C. Shallcross, M. Taddei, J. Wang, G. E. Eperon, N. R. Armstrong, J. J. Berry, D. S. Ginger, *Chem. Mater.* **2021**, 33, 5035.
- [41] D. Kiermasch, L. Gil-Escrig, A. Baumann, H. J. Bolink, V. Dyakonov, K. Tvingstedt, *J. Mater. Chem. A* **2019**, 7, 14712.
- [42] K. Tvingstedt, L. n. Gil-Escrig, C. Momblona, P. Rieder, D. Kiermasch, M. Sessolo, A. Baumann, H. J. Bolink, V. Dyakonov, *ACS Energy Lett.* **2017**, 2, 424.
- [43] Z. S. Wang, F. Ebadi, B. Carlsen, W. C. H. Choy, W. Tress, *Small Methods* **2020**, 4, 2000290.
- [44] W. Shockley, W. Read Jr., *Phys. Rev.* **1952**, 87, 835.
- [45] R. N. Hall, *Phys. Rev.* **1952**, 87, 387.
- [46] T. Kirchartz, J. A. Márquez, M. Stolterfoht, T. Unold, *Adv. Energy Mater.* **2020**, 10, 1904134.
- [47] E. M. Hutter, T. Kirchartz, B. Ehrler, D. Cahen, E. Von Hauff, *Appl. Phys. Lett.* **2020**, 116, 100501.
- [48] B. Krogmeier, F. Staub, D. Grabowski, U. Rau, T. Kirchartz, *Sustainable Energy Fuels* **2018**, 2, 1027.
- [49] L. Krückemeier, B. Krogmeier, Z. Liu, U. Rau, T. Kirchartz, *Adv. Energy Mater.* **2021**, 11, 2003489.
- [50] F. Staub, H. Hempel, J. C. Hebig, J. Mock, U. W. Paetzold, U. Rau, T. Unold, T. Kirchartz, *Phys. Rev. Appl.* **2016**, 6, 044017.
- [51] R. L. Milot, G. E. Eperon, H. J. Snaith, M. B. Johnston, L. M. Herz, *Adv. Funct. Mater.* **2015**, 25, 6218.
- [52] M. J. Trimpl, A. D. Wright, K. Schutt, L. R. V. Buizza, Z. Wang, M. B. Johnston, H. J. Snaith, P. Müller-Buschbaum, L. M. Herz, *Adv. Funct. Mater.* **2020**, 30, 2004312.
- [53] R. A. Sinton, A. Cuevas, *Appl. Phys. Lett.* **1996**, 69, 2510.
- [54] A. Cuevas, R. A. Sinton, *Solar Cells*, (Eds: T. Markvart, L. Castañer), Elsevier Science, Amsterdam **2005**, p. 163.
- [55] E. Palomares, N. F. Montcada, M. Méndez, J. Jiménez-López, W. Yang, G. Boschloo, *Characterization Techniques for Perovskite Solar Cell Materials*, (Eds: M. Pazoki, A. Hagfeldt, T. Edvinsson), Elsevier, **2020**, p. 161.
- [56] Q. Xue, Y. Bai, M. Liu, R. Xia, Z. Hu, Z. Chen, X.-F. Jiang, F. Huang, S. Yang, Y. Matsuo, H.-L. Yip, Y. Cao, *Adv. Energy Mater.* **2017**, 7, 1602333.
- [57] J. Troughton, M. Neophytou, N. Gasparini, A. Seitkhan, F. H. Isikgor, X. Song, Y.-H. Lin, T. Liu, H. Faber, E. Yengel, J. Kosco, M. F. Osajca, B. Hartmeier, M. Rossier, N. A. Lüchinger, L. Tsetseris, H. J. Snaith, S. De Wolf, T. D. Anthopoulos, I. McCulloch, D. Baran, *Energy Environ. Sci.* **2020**, 13, 268.
- [58] S. Toyoshima, K. Kuwabara, T. Sakurai, T. Taima, K. Saito, H. Kato, K. Akimoto, *Jpn. J. Appl. Phys.* **2007**, 46, 2692.
- [59] P. Cui, D. Wei, J. Ji, H. Huang, E. Jia, S. Dou, T. Wang, W. Wang, M. Li, *Nat. Energy* **2019**, 4, 150.
- [60] T. Kirchartz, D. Cahen, *Nat. Energy* **2020**, 5, 973.
- [61] S. Feldmann, S. Macpherson, S. P. Senanayak, M. Abdi-Jalebi, J. P. H. Rivett, G. Nan, G. D. Tainter, T. A. S. Doherty, K. Frohna, E. Ringe, R. H. Friend, H. Sirringhaus, M. Saliba, D. Beljonne, S. D. Stranks, F. Deschler, *Nat. Photonics* **2020**, 14, 123.
- [62] L. Castaner, E. Vilamajo, J. Llaberia, J. Garrido, *J. Phys. D: Appl. Phys.* **1981**, 14, 1867.
- [63] A. Kiligaris, P. A. Frantsuzov, A. Yangui, S. Seth, J. Li, Q. An, Y. Vaynzof, I. G. Scheblykin, *Nat. Commun.* **2021**, 12, 3329.
- [64] J. Siekmann, S. Ravishanker, T. Kirchartz, *ACS Energy Lett.* **2021**, 6, 3244.
- [65] S. Ravishanker, T. Unold, T. Kirchartz, *Science* **2021**, 371, eabd8014.

- [66] P. Calado, A. M. Telford, D. Bryant, X. Li, J. Nelson, B. C. O'Regan, P. R. F. Barnes, *Nat. Commun.* **2016**, *7*, 13831.
- [67] F. Staub, T. Kirchartz, K. Bittkau, U. Rau, *J. Phys. Chem. Lett.* **2017**, *8*, 5084.
- [68] C. v. Berkel, M. J. Powell, A. R. Franklin, I. D. French, *J. Appl. Phys.* **1993**, *73*, 5264.
- [69] P. Caprioglio, C. M. Wolff, O. J. Sandberg, A. Armin, B. Rech, S. Albrecht, D. Neher, M. Stollerfoht, *Adv. Energy Mater.* **2020**, *10*, 2000502.
- [70] O. J. Sandberg, J. Kurpiers, M. Stollerfoht, D. Neher, P. Meredith, S. Shoaee, A. Armin, *Adv. Mater. Interfaces* **2020**, *7*, 2000041.
- [71] B. Das, Z. Liu, I. Aguilera, U. Rau, T. Kirchartz, *Mater. Adv.* **2021**, *2*, 3655.
- [72] M. Azzouzi, P. Calado, A. M. Telford, F. Eisner, X. Hou, T. Kirchartz, P. R. F. Barnes, J. Nelson, *Sol. RRL* **2020**, *4*, 1900581.
- [73] P. R. F. Barnes, K. Miettunen, X. Li, A. Y. Anderson, T. Bessho, M. Gratzel, B. C. O'Regan, *Adv. Mater.* **2013**, *25*, 1881.
- [74] B. C. O'Regan, J. R. Durrant, P. M. Sommeling, N. J. Bakker, *J. Phys. Chem. C* **2007**, *111*, 14001.
- [75] R. Hamilton, C. G. Shuttle, B. O'Regan, T. C. Hammant, J. Nelson, J. R. Durrant, *J. Phys. Chem. Lett.* **2010**, *1*, 1432.
- [76] A. Foertig, J. Rau, V. Dyakonov, C. Deibel, *Phys. Rev. B* **2012**, *86*, 115302.
- [77] C. Shuttle, B. O'Regan, A. Ballantyne, J. Nelson, D. D. Bradley, J. De Mello, J. Durrant, *Appl. Phys. Lett.* **2008**, *92*, 80.
- [78] S. Wood, J. C. Blakesley, F. A. Castro, *Phys. Rev. Appl.* **2018**, *10*, 024038.
- [79] Z. Liu, L. Krückemeier, B. Krogmeier, B. Klingebiel, J. A. Márquez, S. Levchenko, S. Öz, S. Mathur, U. Rau, T. Unold, T. Kirchartz, *ACS Energy Lett.* **2019**, *4*, 110.
- [80] I. Levine, S. Gupta, A. Bera, D. Ceratti, G. Hodes, D. Cahen, D. Guo, T. J. Savenije, J. Ávila, H. J. Bolink, O. Millo, D. Azulay, I. Balberg, *J. Appl. Phys.* **2018**, *124*, 103103.
- [81] D. Credgington, J. R. Durrant, *J. Phys. Chem. Lett.* **2012**, *3*, 1465.
- [82] A. Richter, S. W. Glunz, F. Werner, J. Schmidt, A. Cuevas, *Phys. Rev. B* **2012**, *86*, 165202.
- [83] U. Rau, T. Kirchartz, *Adv. Mater. Interfaces* **2019**, *6*, 1900252.
- [84] U. Rau, V. Huhn, B. E. Pieters, *Phys. Rev. Appl.* **2020**, *14*, 014046.
- [85] C. Sah, R. N. Noyce, W. Shockley, *Proc. IRE* **1957**, *45*, 1228.